

JGR Solid Earth

RESEARCH ARTICLE

10.1029/2024JB029410

Key Points:

- We perform a joint seismo-geodetic dynamic rupture and afterslip inversion of the 2004 Parkfield event
- We find that coseismic rupture is separated into a strongly radiating pulse-like and a mildly radiating crack-like phase
- Distinct dynamic rupture arrest mechanisms imprint on afterslip evolution and afterslip may drive delayed aftershocks

Supporting Information:

Supporting Information may be found in the online version of this article.

Correspondence to:

N. Schliwa,
nico.schliwa@lmu.de

Citation:

Schliwa, N., Gabriel, A.-A., Premus, J., & Gallovič, F. (2024). The linked complexity of coseismic and postseismic faulting revealed by seismo-geodetic dynamic inversion of the 2004 Parkfield earthquake. *Journal of Geophysical Research: Solid Earth*, 129, e2024JB029410. <https://doi.org/10.1029/2024JB029410>

Received 26 APR 2024

Accepted 21 NOV 2024

Author Contributions:

Conceptualization: Alice-Agnes Gabriel, František Gallovič

Data curation: Nico Schliwa, Jan Premus

Formal analysis: Nico Schliwa, Jan Premus

Funding acquisition: Alice-Agnes Gabriel, František Gallovič

Investigation: Nico Schliwa, Alice-Agnes Gabriel, Jan Premus, František Gallovič

Methodology: Jan Premus, František Gallovič

Project administration: Alice-Agnes Gabriel, František Gallovič

Software: Jan Premus, František Gallovič

© 2024 The Author(s).

This is an open access article under the terms of the [Creative Commons Attribution-NonCommercial License](https://creativecommons.org/licenses/by-nc/4.0/), which permits use, distribution and reproduction in any medium, provided the original work is properly cited and is not used for commercial purposes.

The Linked Complexity of Coseismic and Postseismic Faulting Revealed by Seismo-Geodetic Dynamic Inversion of the 2004 Parkfield Earthquake

Nico Schliwa¹ , Alice-Agnes Gabriel^{1,2} , Jan Premus³ , and František Gallovič⁴ 

¹Ludwig-Maximilians-Universität München, Munich, Germany, ²Scripps Institution of Oceanography, UC San Diego, CA, USA, ³Côte d'Azur University, Nice, France, ⁴Charles University, Prague, Czech Republic

Abstract Several regularly recurring moderate-size earthquakes motivated dense instrumentation of the Parkfield section of the San Andreas fault (SAF), providing an invaluable near-fault observatory. We present a seismo-geodetic dynamic inversion of the 2004 Parkfield earthquake, which illuminates the interlinked complexity of faulting across time scales. Using fast-velocity-weakening rate-and-state friction, we jointly model coseismic dynamic rupture and the 90-day evolution of postseismic slip in a 3D domain. We utilize a parallel tempering Markov chain Monte Carlo approach to solve this non-linear high-dimensional inverse problem, constraining spatially varying prestress and fault friction parameters by 30 strong motion and 12 GPS stations. From visiting >2 million models, we discern complex coseismic rupture dynamics that transition from a strongly radiating pulse-like phase to a mildly radiating crack-like phase. Both coseismic phases are separated by a shallow strength barrier that nearly arrests rupture and leads to a gap in the afterslip, reflecting the geologic heterogeneity along this segment of the SAF. Coseismic rupture termination involves distinct arrest mechanisms that imprint on afterslip kinematics. A backward propagating afterslip front may drive delayed aftershock activity above the hypocenter. Trade-off analysis of the 10,500 best-fitting models uncovers local correlations between prestress levels and the reference friction coefficient, alongside an anticorrelation between prestress and rate-state parameters $b - a$. We find that a complex, fault-local interplay of dynamic parameters determines the nucleation, propagation, and arrest of both, co- and postseismic faulting. This study demonstrates the potential of inverse physics-based modeling to reveal novel insights and detailed characterizations of well-recorded earthquakes.

Plain Language Summary The Parkfield section of the San Andreas plate boundary hosts regularly recurring moderate-size earthquakes. Seismic ground motions and slow deformation following the 2004 Parkfield earthquake were recorded by more than 40 seismometers and 13 GPS stations. While this is arguably one of the best-recorded earthquakes, it remains challenging to constrain the physics and properties at depth governing the earthquake from surface observations. Data-driven earthquake models solving inverse problems usually describe the kinematics of rupture. Here, we employ a computationally expensive numerical algorithm to invert observations dynamically and find a physics-based set of parameters that simultaneously explain the earthquake and its afterslip, slow deformation following an earthquake. We find two separate phases of the earthquake that cause a similar amount of permanent displacement, but the rapid rupture of the first phase radiates much more potentially damaging seismic waves. The permanent displacement caused by the afterslip of the 2004 Parkfield earthquake exceeded its coseismic displacement. The local frictional properties that arrest the earthquake imprint on the subsequent afterslip evolution. Our approach illustrates that physics-based models utilizing modern computing techniques can reveal new insights and unprecedented detail even of well-studied events.

1. Introduction

The Parkfield section marks the transition between a locked part of the main strand of the San Andreas Fault (SAF) system and a creeping section to the northwest, with slip rates of 20–30 mm/yr (Jolivet et al., 2015; Titus et al., 2005; Tong et al., 2013). The transition between the creeping and locked sections is approximately at Middle Mountain (Murray & Langbein, 2006). Several earthquakes of $M_w \approx 6$ struck the Parkfield section in 1857, 1881, 1901, 1922, 1934, and 1966, corresponding to an average recurrence time of 22 ± 3 years (Bakun & McEvilly, 1984). The Parkfield earthquake prediction experiment (Bakun & Lindh, 1985) anticipated another $M_w \approx 6$

Supervision: Alice-Agnes Gabriel, František Gallovič
Validation: František Gallovič
Visualization: Nico Schliwa
Writing – original draft: Nico Schliwa, Alice-Agnes Gabriel, Jan Premus, František Gallovič

earthquake in 1988 ± 5 years and motivated dense seismic and geodetic instrumentation in the area. However, the anticipated Parkfield earthquake only happened in 2004 without noticeable short-term precursory signals (Bakun et al., 2005; Bilham, 2005). More than 40 strong-motion instruments and 13 GPS stations (Figure 1) recorded the 2004 Parkfield earthquake and its afterslip within an epicentral distance of less than 32 km (e.g., Johnson et al., 2006; Liu et al., 2006).

1.1. Kinematic Source Inversion and Back-Projection Imaging

Kinematic source inversions and back-projection studies of the 2004 Parkfield earthquake reveal a heterogeneous rupture process regarding slip, rupture speed, and rise time. The inferred kinematic models generally agree that the rupture process was complex despite its moderate size, with coseismic slip mainly confined within a depth range of 4–10 km (e.g., Langbein et al., 2006). Most models suggest a primary high slip patch surrounding the hypocenter and a second major slip area, 15–20 km northwest of the hypocenter (Custódio et al., 2009; Johanson et al., 2006; Liu et al., 2006; Twardzik et al., 2012), with purely geodetic models being generally smoother (Kim & Dreger, 2008; Page et al., 2009). Some studies (Custódio et al., 2009; Fletcher et al., 2006) concluded that there was rapid rupture onset with rupture velocities close to the S-wave speed (≈ 3.6 km/s at hypocentral depth) and rise times shorter than 1 s. Propagating to the northwest, rupture speed may have decreased and rise times increased (Custódio et al., 2009; Fletcher et al., 2006; Ma et al., 2008).

Data-driven, kinematic earthquake models use various data sets to illuminate the space-time evolution of both coseismic rupture and afterslip. Still, they typically cannot probe dynamically consistent pre-, co-, and post-seismic mechanical conditions of faulting. Dynamic rupture forward modeling, on the other hand, is typically limited to the coseismic timescale and compares simulation results selectively to observational data or kinematic models (e.g., Taufiqurrahman et al., 2023; Tinti et al., 2021; Ulrich et al., 2019; Wen et al., 2024).

1.2. Results From Previous Dynamic Modeling

Several studies investigated the dynamic source process of the 2004 Parkfield earthquake. Ma et al. (2008) constructed a dynamic rupture forward model using a linear slip-weakening friction law with mostly uniform frictional properties and a constant seismic S parameter (Andrews, 1976) for regions with a positive stress drop. S is the ratio of the strength excess over the expected stress drop, $S = \frac{\tau_y - \tau_0}{\tau_0 - \tau_d}$, where τ_y is the yield stress ($\sigma_n \mu_s$), τ_0 is the initial stress, and τ_d is the dynamic frictional stress ($\sigma_n \mu_d$). μ_s and μ_d are the static and dynamic friction coefficients, respectively. Their spatial distribution of the initial stress τ_0 is initially informed by a kinematic slip model (Custódio et al., 2005). They successively modify the initial stresses, τ_0 , and choose the S parameter and the characteristic slip-weakening distance D_c by trial and error to match near-source ground motions.

Twardzik et al. (2014) performed a simple dynamic inversion to constrain the dynamic parameters that governed coseismic rupture. They assumed that the slip was confined to two elliptical patches and inverted for the geometry of the patches, the maximum S parameter within the patches, and the uniform background frictional properties of the fault plane. Barbot et al. (2012) created a long-term fully dynamic seismic cycle simulation of the Parkfield section, using a Dieterich-Ruina aging rate-and-state friction law (Dieterich, 1992; Ruina, 1983). They prescribed a heterogeneous spatial distribution of the difference between the friction parameters a and b , determining velocity-strengthening (VS) and velocity-weakening (VW) behavior. All other friction parameters were kept constant. Their model reproduced an earthquake sequence of irregular M_w 6.0 mainshocks with varying propagation directions. Kostka and Gallovič (2016) modified the dynamic model of Barbot et al. (2012) and showed that a stress perturbation, possibly caused by the nearby 1983 Coalinga-Nuñez earthquakes, may have delayed the occurrence of the 2004 Parkfield mainshock.

1.3. Afterslip and Aftershocks

An extended period of exceptionally large postseismic deformation followed the 2004 Parkfield earthquake. At the surface, the San Andreas fault zone at Parkfield consists of two main fault branches, the main SAF and the Southwest Fracture Zone (SWFZ), which are likely connected below 6 km depth (Simpson et al., 2006). During the 2004 Parkfield earthquake, the SWFZ ruptured coseismically. The SAF slipped postseismically, and afterslip at the surface was detected only hours after the event (Jiang et al., 2021a; Langbein et al., 2006; Lienkaemper et al., 2006; Rymer et al., 2006). Murray and Langbein (2006) estimated the moment of the postseismic slip during

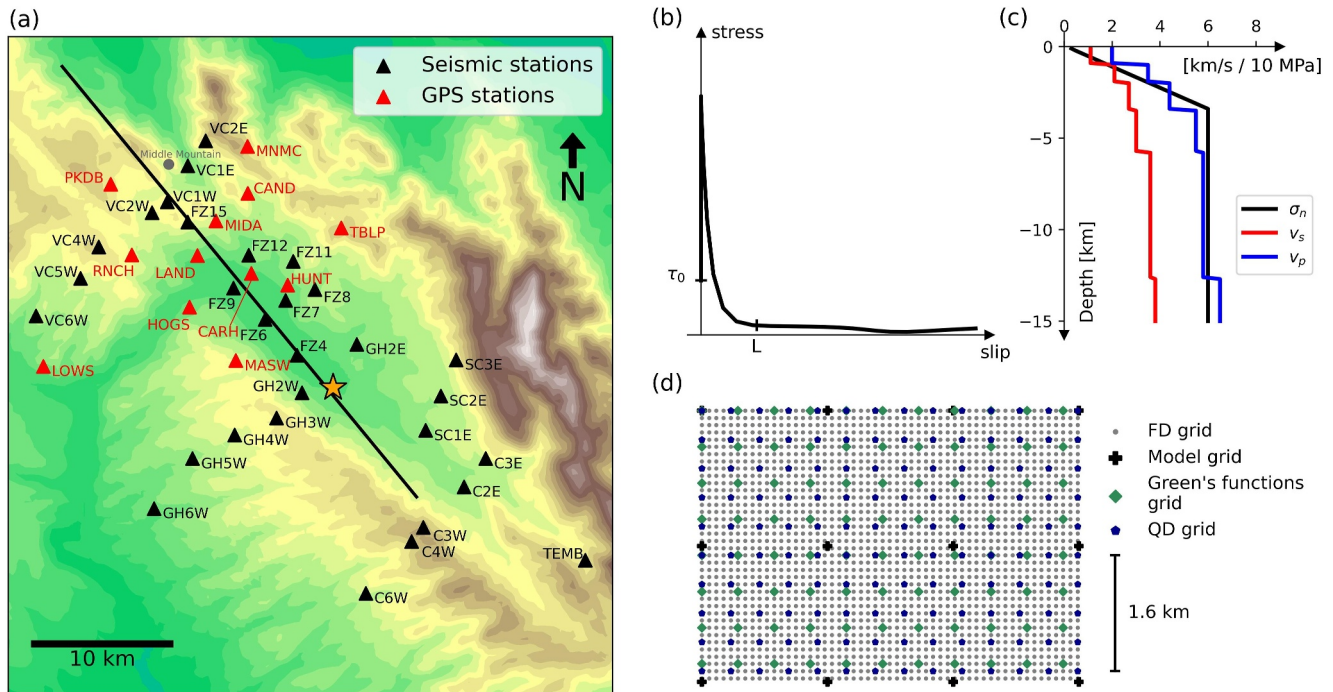


Figure 1. (a) Map view of the model domain with near-fault stations utilized in the dynamic inversion. Black triangles show seismic stations, red triangles are GPS stations, the black line is the fault trace, and the star marks the epicenter location. Topography is shown for regional context but is not accounted for in our forward models. (b) Exemplary stress evolution during coseismic dynamic rupture governed by the fast-velocity-weakening rate-and-state friction law measured in one of our dynamic rupture simulations. τ_0 represents the prestress and L the characteristic slip distance. (c) Assumed depth-dependent normal stress σ_n and averaged seismic velocity profile used in the finite difference solver. We use two different seismic velocity profiles to compute different Green's functions for each side of the fault, respectively, following Custódio et al. (2005). (d) Illustration of the four different grids discretizing the fault plane used in the dynamic source inversion. Dynamic model parameters are defined on the coarsest grid (model grid, black crosses) and bilinearly interpolated on the finest grid used in the finite-difference dynamic rupture solver (FD grid, gray dots) and the grid used in the quasi-dynamic boundary element method (QD grid, blue dots). Slip rates and slip from the FD or QD grids are averaged on the Green's functions grid (green dots) to compute synthetic seismograms and GPS displacements.

the first 60 days following the earthquake to be 2×10^{18} Nm, which is larger than the coseismic moment release of 1.3×10^{18} Nm. Postseismic slip occurred mainly above the coseismic rupture zone and further to the northwest (Johanson et al., 2006; Langbein et al., 2006). Surface afterslip reached 20–30 cm one year after the earthquake (Lienkaemper et al., 2006). Barbot et al. (2009) demonstrated that a purely rate-strengthening friction law applied on a planar fault can explain most of the observed postseismic surface displacements. Jiang et al. (2021a) combined high-rate with daily GPS solutions to study the early afterslip of the 2004 Parkfield event and found that early afterslip-associated stress changes appear synchronized with local aftershock rates.

Stress changes induced by coseismic slip and/or afterslip have been proposed to drive aftershock activity (e.g., Churchill et al., 2024). The 2004 Parkfield aftershocks appear mainly concentrated in two near horizontal streaks bordering the coseismic rupture zone, one between 4 and 6 km depth and the other one between 8 and 10 km depth (Thurber et al., 2006). Seismicity migrated along-strike and along-dip during the months after the earthquake, which has been interpreted as an indication of afterslip acting as the main driver of aftershocks (Jiang et al., 2021a; Peng & Zhao, 2009). However, Cattania et al. (2015) suggest that secondary triggering of aftershocks by earlier aftershocks may have played a more important role, and Churchill et al. (2022)'s global statistical analysis found no correlation between the relative afterslip moment and large aftershock activity.

1.4. Dynamic Earthquake Source Inversion

The benefits of inverting for dynamic parameters to construct physically consistent source models have been recognized long ago (Fukuyama & Mikumo, 1993; Peyrat & Olsen, 2004; Twardzik et al., 2014), and recent advances in computational capabilities enable inverting for multiple spatial-variable dynamic parameters. Gallovič et al. (2019a) established a Bayesian dynamic source inversion framework, constraining the spatially variable linear slip-weakening friction dynamic parameters (fault prestress, strength and characteristic slip-

weakening distance) across a finite, planar fault. This method has been applied to the 2016 M_w 6.2 Amatrice (Galović et al., 2019b) and 2020 M_w 6.8 Elazığ earthquake (Galović et al., 2020), using strong ground motion observations to constrain dynamic rupture parameters and quantify their uncertainties. Premus et al. (2022) extended the method to rate-and-state friction, which enables jointly simulating coseismic slip and afterslip in the same framework. Their dynamic source inversion of the 2014 M_w 6.0 South Napa California earthquake constrained by co- and postseismic strong ground motion and GPS data illuminated how variable prestress and frictional conditions on the fault govern the spatial separation between shallow coseismic and postseismic slip, the progression of afterslip driving deep off-fault aftershocks, and the coseismic slip distribution.

Here, we apply the approach introduced in Premus et al. (2022) to the extensive seismic and geodetic observations of the 2004 Parkfield earthquake. We are especially interested in investigating the interrelation of coseismic slip and the exceptionally large amount of afterslip in a uniform, data-driven modeling framework. We jointly invert this data to establish an ensemble of dynamic models that simultaneously describe the coseismic and 3 months of postseismic slip evolution. We detail the complex coseismic and postseismic faulting dynamics of a preferred joint model. We find new evidence for the coseismic rupture phase involving distinctly different rupture styles and explore the complex fault slip transition from the coseismic to the postseismic phase. We investigate which dynamic parameters govern different coseismic and afterslip rupture styles and analyze trade-offs between the dynamic parameters. Additionally, we observe that different mechanisms for terminating coseismic rupture leave distinct imprints on afterslip evolution. We jointly quantify the average values and variability of coseismic source characteristics, including stress drop, fracture energy, and radiation efficiency, as well as afterslip kinematics such as rise time, propagation speed, and spatial heterogeneity and extent based on physics-based and data-driven models.

2. Methods

This section summarizes the forward and inverse modeling methods and seismic and geodetic data sets used in this study. We present the two stages of our forward model and the respective numerical solvers. Then, we detail the data used to constrain the inversion and our model parameterization. Lastly, we present our inversion strategy. We introduce the friction law that facilitates the dynamic description of our problem and our Parallel Tempering Markov chain Monte Carlo Bayesian inversion method in the Supplementary Information (Texts S1 and S2 in Supporting Information S1).

2.1. Joint Dynamic Rupture and Afterslip Forward Model

The forward model consists of two stages, the coseismic and the postseismic phase, implemented using a 3D fully dynamic and a 3D quasi-dynamic method, respectively (Premus et al., 2022). In the coseismic stage, we model the earthquake dynamic rupture propagation with the code FD3D_TSN (Premus et al., 2020) based on an efficient GPU implementation of a finite-difference method. The code uses a fourth-order accurate staggered-grid method with a traction-at-split node implementation (Dalguer & Day, 2007) of the frictional fault interface condition.

The postseismic phase is modeled with a 3D quasi-dynamic boundary element approach (Galović, 2008). The method solves the elastodynamic equation but replaces the inertial term with a radiation damping term (Rice, 1993), facilitating complex afterslip effects such as migrating afterslip fronts. We solve the quasi-dynamic problem with a fifth-order Runge-Kutta method with adaptive time stepping. Both stages share the same planar fault geometry and the same distribution of dynamic parameters but will be constrained by complementary observations. The final coseismic distributions of the shear stress, slip rate, and state variable are used as the initial values of the postseismic stage. Synthetic seismograms and static displacements are calculated via precomputed Green's functions (Cotton & Coutant, 1997; Okada, 1985).

3D dynamic rupture simulations are computationally expensive, and using rate-and-state friction laws increases this cost compared to linear-slip weakening friction (e.g., Heinecke et al., 2014; Krenz et al., 2021; Uphoff et al., 2017). Monte-Carlo-based Bayesian inversion approaches require many forward models (e.g., Press, 1968). Therefore, our joint dynamic coseismic and afterslip inversion requires large computational resources. The coseismic dynamic rupture propagation stage spans the first 21 s of the forward model, after which slip rates are low enough ($<10^{-2}$ m/s) to switch to the quasi-dynamic simulation in the postseismic stage lasting for 90 days. We use a finite-difference grid spacing of 100 m (Figure 1d), which sufficiently samples the critical length scale

of dynamic rupture, the process zone at the rupture tip, with an average of 6.3 points, ensuring accuracy (Day et al., 2005). The grid spacing of the quasi-dynamic solver is 400 m.

2.2. Seismic and Geodetic Data

We include seismic and geodetic measurements, both on coseismic and postseismic time scales, as inversion data. To constrain the coseismic rupture dynamics, we use strong-motion observations at 30 near-fault stations (Figure 1a). We excluded several near-fault stations due to missing origin times, strong fault zone effects apparent even at low frequencies, or pronounced site amplifications (Liu et al., 2006). We include only horizontal components due to the worse signal-to-noise ratio of vertical components and because we do not allow for dip-slip (see Section 2.3). De-emphasizing vertical components is a common assumption for strong-motion inversions of the 2004 Parkfield strike-slip earthquake, for example, Liu et al. (2006) down-weighted the vertical components by a factor of 10. The strong-motion data is integrated to velocities and filtered by a fourth-order causal Butterworth filter between 0.16 and 0.5 Hz. We choose a low-frequency limit of 0.16 Hz to ensure a flat frequency response of all instruments (Custódio et al., 2005). The chosen upper limit of 0.5 Hz mitigates the impact of the 3D velocity structure, in particular, of the low-velocity fault zone, which may affect all near-fault stations (Lewis & Ben-Zion, 2010; Li et al., 1990). We use 25 s long seismic waveforms during the convergence phase (see Section 2.4). In the subsequent sampling phase, we limited the coseismic waveforms to 15 s long waveforms. The chosen relatively short time windows of 25 s or 15 s reduce contamination from seismic reverberations due to the 3D subsurface structure. We assume a universal data uncertainty of $\sigma = 0.05$ m/s when computing the posterior probability density function of the data (Equation S7 in Text S2 in Supporting Information S1). The assumed data uncertainty corresponds to approximately half of the maximum data amplitude, in agreement with estimates derived from numerical experiments involving randomly varied velocity models (Hallo & Gallovič, 2016).

We use the preprocessed horizontal GPS data by Jiang et al. (2021a) that span both coseismic and postseismic periods. Namely, we include the coseismic displacements at 12 GPS stations (Figure 1a) and postseismic displacements at 11 GPS stations during the 90-day postseismic period. We compare the postseismic observations with our synthetics at 35 logarithmically spaced points in time to increase the weight and resolution of the early afterslip phase. We excluded the postseismic data from the GPS station CARH as it is located between the main trace of the SAF and the secondary SWFZ branch southwest of the SAF. Afterslip migrating from the SWFZ to the SAF likely led to the polarity change of the postseismic deformation measured at CARH (Jiang et al., 2021a; Murray & Langbein, 2006), an effect which our single fault model cannot capture. We completely exclude the GPS station POMM from our analysis since it is located directly above the SWFZ and is likely strongly affected by small-scale complexities in fault geometry that we cannot capture in our planar fault model (Custódio et al., 2009; Murray & Langbein, 2006). We assign an individual uncertainty value to each GPS station calculated from the mean of the data uncertainty as given by Jiang et al. (2021a) during the included 90-day period.

2.3. Model Setup

Our dynamic rupture and afterslip forward model incorporates a single planar fault with a strike of 320.5° and dip of 87.2° based on the fault geometry of the SWFZ of Jiang et al. (2021a). The Green's functions account for the fault dip, but the dynamic rupture and quasi-dynamic models assume a vertical fault plane similar to (Gallovič et al., 2019a, 2019b; Premus et al., 2022). We place the hypocenter in the initial dynamic rupture model at 35.8154°N , 120.3667°W , and 7.5 km depth based on a matched filter relocated earthquake catalog (Neves et al., 2022). We use two different 1D velocity profiles (Custódio et al., 2005) to calculate Green's functions accounting for different materials on each side of the fault (Table S1 in Supporting Information S1). The coseismic dynamic rupture model assumes an average of both 1D layered velocity profiles, while the postseismic model assumes a homogenous medium, with $v_s = 3600$ m/s, $v_p = 5800$ m/s, and $\rho = 2700$ kg/m³. Using the homogeneous half-space assumption enables efficient computation of stresses by convolution accelerated by the 2D Fourier transform (Gallovič, 2008). However, this approach reduces accuracy, particularly if the actual medium has layers with contrasting mechanical properties. Future studies should explore static Green's functions for layered and 3D material models (e.g., Uphoff et al., 2022; Wang et al., 2003, 2006) for computing stress redistribution and static displacements. The coseismically used Green's functions account for anelastic attenuation. We assume variable Q values based on an empirical relationship with v_s : $Q_s = 0.1 v_s$ (in m/s) and $Q_p = 1.5 Q_s$ (Olsen et al., 2003).

Table 1
Minimum and Maximum Values of the Dynamic Parameters Subject to the Inversion

Label	Parameters	Minimum value	Maximum value
τ_0	Shear prestress	10^3 Pa	2×10^9 Pa
$b - a$	Difference between the state evolution and the direct effect parameter	-0.03	0.03
f_0	Reference friction coefficient at $\dot{s}_0 = 10^{-6}$ m/s	0.2	1.5
L	Characteristic slip distance	0.004 m	1.0 m
\dot{s}_w	Weakening slip rate	0.01 m/s	2.0 m/s
\dot{s}_{init}	Initial slip rate	10^{-13} m/s	1.21×10^{-9} m/s
h_x	Along-strike position of nucleation patch	28.0 km	32.0 km
h_z	Along-dip position of nucleation patch	6.5 km	9.0 km
r_{nuc}	Radius of the nucleation patch	225 m	450 m
σ_{nuc}	Stress increase within the nucleation patch	1%	60%

Note. \dot{s}_w and \dot{s}_{init} can only vary in the velocity-strengthening areas of the fault and have constant values of 0.1 m/s and 10^{-12} m/s in the velocity-weakening areas, respectively.

Table 1 summarizes the six dynamic parameters ($\tau_0, b - a, f_0, L, \dot{s}_w, \dot{s}_{init}$) and four coseismic rupture nucleation parameters ($h_x, h_z, r_{nuc}, \sigma_{nuc}$) subject to Bayesian inversion. We fix the weakened friction coefficient f_w to a constant value of $f_w = 0.3$ following Ma et al. (2008) and vary only the reference friction coefficient f_0 , and, thereby, the “reference friction drop”, $f_0 - f_w$. Similarly, we fix the direct effect parameter a to a constant value of $a = 0.015$ and allow the state evolution parameter b to vary, altering the difference $b - a$. We assume pure strike-slip faulting without dip-slip. Thus, the prestress τ_0 and the initial slip rate \dot{s}_{init} are scalars. The dynamic parameters (prestress and friction parameters) are defined on the model grid with 24 points along-strike and 9 points along-dip (Figure 1d). In between the grid points, the dynamic parameters are bilinearly interpolated on the denser FD (finite-difference) and QD (quasi-dynamic) grids. The outermost model grid points align with the fault edges, ensuring well-defined bilinear interpolation across the entire fault. The such defined number of potentially free dynamic inversion parameters is 1,300. However, the weakening slip rate \dot{s}_w and \dot{s}_{init} can only vary in the VS areas of the fault and have constant values of 0.1 m/s and 10^{-12} m/s in the VW areas, respectively. The constant \dot{s}_w and \dot{s}_{init} in the VW regions simulate locked asperities. Therefore, the number of effectively free parameters is approximately 1,100 and can dynamically change throughout the inversion.

We use a temporary (for 1 s) overstressed nucleation patch around the hypocenter to initiate dynamic rupture. We invert for the radius of this nucleation patch and the associated shear stress increase. The along-strike and along-dip location of the center of the nucleation patch, the hypocenter, is also subject to the inversion (see Table 1).

The effective normal stress linearly increases until a depth of 3.5 km (Figure 1c) and then remains constant at 60 MPa at deeper depths (Madden et al., 2022; Rice, 1992; Suppe, 2014), reflecting the transition from a hydrostatic to a lithostatic pore fluid pressure gradient. Our profile is similar to the normal stress profile in a previous 2004 Parkfield dynamic rupture forward model (Ma et al., 2008).

2.4. Inversion Strategy

Dynamic source inversion is challenging due to the nonlinear, ill-posed nature of the very high-dimensional problem and the complicated non-convex shape of the misfit function. We aim to increase the inversion's performance by choosing an initial model (IM) with a high probability density (close to the optimal model). We split the dynamic inversion workflow into a convergence phase and a sampling phase. The latter generates the ensemble for uncertainty quantification. During the convergence phase, we manually modify model parameters, adjust weights and data sets, and restart the Markov chains to achieve faster convergence. Thus, only the sampling phase represents an undisturbed MCMC inversion. The maximum likelihood model of the convergence phase serves as the starting model of the sampling phase. Only a few Markov chain links separate this starting model

from our preferred model (PM) (Section 3.2). A diagram illustrating the dynamic source inversion approach is provided in the Supporting Information (Figure S1 in Supporting Information S1).

A randomly chosen IM may not nucleate self-sustained rupture or produce a much larger moment magnitude than the target earthquake. Therefore, we construct an initial dynamic rupture model based on the stress drop and final slip distribution of “Model B” of Ma et al. (2008), who use linear slip-weakening friction to model the coseismic rupture of the 2004 Parkfield earthquake. We choose the prestress τ_0 distribution of our IM to resemble the final slip distribution of Ma et al. (2008). Then, we adapt our reference friction f_0 and the characteristic slip distance L to approximately reproduce their rupture velocity distribution using a few trial-and-error simulations. In addition, we randomly perturb the characteristic slip distance L and the prestress τ_0 by up to $\pm 10\%$ to include small-scale heterogeneity and rupture complexity (see Figure S2 in Supporting Information S1). Ma et al. (2008) prefer their Model B over their Model A because Model B generates surface displacements more consistent with GPS observations and its slip distribution is more consistent with aftershock locations. For the same reasons, we select their Model B to construct our IM.

Despite the random perturbations, the rupture of the IM is very homogeneous (Figure S3 in Supporting Information S1). The IM's fit to the data is moderate (see Figures S4 and S5 in Supporting Information S1). It yields a

seismic variance reduction of 0.04 and a coseismic GPS variance reduction of 0.87 ($VR = 1 - \frac{\sum_{i=1}^N \|\mathbf{s}_i(\mathbf{m}) - \mathbf{d}_i\|^2}{\sum_{i=1}^N \|\mathbf{d}_i\|^2}$, \mathbf{d}_i are the observed data, $\mathbf{s}_i(\mathbf{m})$ are the synthetics, and N is the total number of stations).

The first $\approx 500,000$ models generated during the convergence phase focus on the coseismic dynamic rupture phase (21 s) and 69 s of early afterslip. Then, we modify the best-fit model from this convergence ensemble to capture long-term (90-day) afterslip observations. We manually increase the initial slip rate and prestress in certain VS areas to approximately match the afterslip distribution of Jiang et al. (2021a) and the GPS-only model of Johanson et al. (2006). To suppress anomalously high afterslip at the free surface, we set the reference friction coefficient to 1.2 and the prestress below 1 MPa at the free surface's model grid points.

The convergence phase, including long-term afterslip, additionally visits $\approx 700,000$ models. During the convergence phase, we adjust the weighting of the different data sets (strong-motion, coseismic GPS, and postseismic GPS) to ensure their respective misfits remain of the same order of magnitude. Similarly, we successively reduce the step size of the inversion parameter perturbations to keep the model acceptance rate above 10% (Table S2 in Supporting Information S1). We restart the Markov chains several times after finding a model with a significantly improved misfit. This model then serves as a new starting model for all otherwise independent MPI ranks of the inversion algorithm (see Text S2 in Supporting Information S1).

We start the sampling phase after reaching a satisfying data misfit. In this final phase representing a true MCMC inversion, we let the chains sample the model space without manual interventions to obtain an ensemble of best-fitting models that can explain the data similarly well. The final sampling phase of the inversion visits $\approx 800,000$ models. The resulting best-fitting model ensemble contains 10,500 unique models. During the sampling phase, all inversion meta-parameters are kept constant.

We run the inversion on a server with 8 Nvidia RTX A5000-GPUs and 32 AMD-EPYC-7313 CPU cores with a 3 GHz base frequency. We compute the coseismic stage on the GPUs and the postseismic stage on the CPUs. This hybrid approach allows us to exploit the hardware architecture efficiently using 24 MPI ranks (3 ranks per GPU). One simulation of the joint forward model takes, on average, 3 min for the coseismic phase and 2 min for the postseismic phase, totaling 5 min. Therefore, we can visit, on average, 4.8 joint forward models per minute. Overall, the inversion visited more than 2 million joint simulations. This sums up to over 300 days of runtime on our server or $>57,000$ hr on a single GPU.

3. Results

3.1. Initial Dynamic Rupture Model

Our initial dynamic rupture model (IM), which is extended from the dynamic rupture model by Ma et al. (2008), already reveals interesting dynamic aspects of the 2004 Parkfield rupture. We find that an unusually low potential stress drop ($\tau_0 - \sigma_n f_w$) and reference friction drop ($f_0 - f_w$) are needed to match the large-scale rupture characteristics of the 2004 Parkfield earthquake. However, in the rate-and-state framework, both parameters are only

approximations of the actual stress drop and friction drop ($f_{\max} - f_{\min}$). The earthquake ruptured over an area larger than 20 km along strike while coseismic slip remained mostly below 25 cm, which is small considering its magnitude of M_w 6.0 (Bregman et al., 2019) and in agreement with previous observational studies (e.g., Custódio et al., 2009; Liu et al., 2006). The IM requires a low average potential stress drop to facilitate dynamic rupture across a wide area with a small average slip. Differences in the dynamic parameters in our IM compared to Ma et al. (2008), who use linear slip-weakening friction, arise from the distinct friction laws. For example, the additional weakening at high slip rates in our friction law permits rupture propagation at lower prestress levels (Thomas et al., 2014), resulting in smaller potential stress drops. In the IM, we set the potential stress drop to 3.0 MPa within the hypocentral area and to only 0.6 MPa elsewhere, where we expect coseismic rupture (see Figure S6 in Supporting Information S1). Outside of the expected rupture area, the potential stress drop gradually decreases to -3.0 MPa.

A lower stress drop generally reduces rupture velocity (Andrews, 1976; Gabriel et al., 2012). However, several studies observed that the average rupture velocity of the 2004 Parkfield earthquake is relatively fast at 2.5–3.5 km/s (e.g., Custódio et al., 2009; Fletcher et al., 2006; Ma et al., 2008). To achieve a dynamic rupture model that combines a low stress drop with moderate-to-high rupture velocity, we set the characteristic slip distance within the coseismic rupture area to a value of $L = 2$ cm and assume a small S parameter.

We compute the S parameter as $S = \frac{f_0 \sigma_n - \tau^0}{\tau^0 - f_w \sigma_n}$, which represents only an approximation because the minimum and maximum friction coefficients are dynamically determined in rate-and-state friction (Gabriel et al., 2012). Our L is smaller than D_c from the dynamic rupture model by Ma et al. (2008). An equivalent D_c might potentially be inferred from our L parameter if a proper scaling relation (Cocco & Bizzarri, 2002) could be derived for the fast-velocity weakening rate-and-state friction law. Since the weakened friction coefficient ($f_w = 0.3$) and the potential stress drop are already prescribed in the IM, we choose a small reference friction $f_0 = 0.313$. This leads to a reference friction drop of only 0.013, which is unusually low compared to common dynamic rupture simulation parameterizations (e.g., 0.4 in Harris et al., 2018). However, such a small reference friction value is in line with results obtained from dynamic modeling of afterslip following the 2004 Parkfield earthquake (Chang et al., 2013).

3.2. Preferred Joint Dynamic Rupture and Afterslip Model

Next, we present our preferred joint dynamic rupture and afterslip model (PM) in terms of coseismic and postseismic rupture characteristics, fit to the seismic and geodetic observations, and distribution of dynamic parameters. We chose the PM, which is a joint dynamic rupture and 90-day afterslip simulation, to maximize the sum of the seismic and combined (coseismic + postseismic) GPS data variance reductions (VR). The PM model selected by this criterion achieves a better seismic fit compared to the maximum likelihood model of the inversion.

3.2.1. Dynamic Parameters of the Preferred Joint Dynamic Rupture and Afterslip Model

Figure 2 shows the six dynamic parameters of our PM, which are subject to the inversion. We do not show parameters on those parts of the faults that we consider unconstrained by the inversion due to the fact that the sum of the co- and postseismic slip amplitudes remains too small. We note that dynamic parameters below the coseismic rupture extent are less well constrained due to the limited afterslip and low GPS sensitivity.

3.2.1.1. Prestress, Velocity-Weakening and Velocity-Strengthening Friction

The spatial average of the prestress within the coseismic rupture area is 18.6 MPa with a standard deviation of 3.4 MPa. We define the coseismic rupture area as the region where coseismic slip exceeds 0.01 m, and the fault slip area as the region where the overall slip (coseismic + postseismic) exceeds 0.1 m within a radius of 1.2 km (visible area in Figure 2). The fault slip area also includes well-constrained strength barriers. When considering the fault slip area, the spatial average prestress reduces to 14.9 MPa, and the standard deviation increases to 6.6 MPa.

Within the coseismic rupture area, $b - a$ remains dominantly positive, which is associated with VW behavior. The spatial average value is 0.0037, and the standard deviation is 0.0048. The standard deviation being larger than its average is associated with the dynamic rupture penetrating the shallowest portion of the fault where $b - a$ is negative. For the fault slip area, including regions hosting afterslip, the spatial average of $b - a$ drops to 0.000 with a standard deviation of 0.0059. The respective $b - a$ averages in the VS and VW regions are comparable to

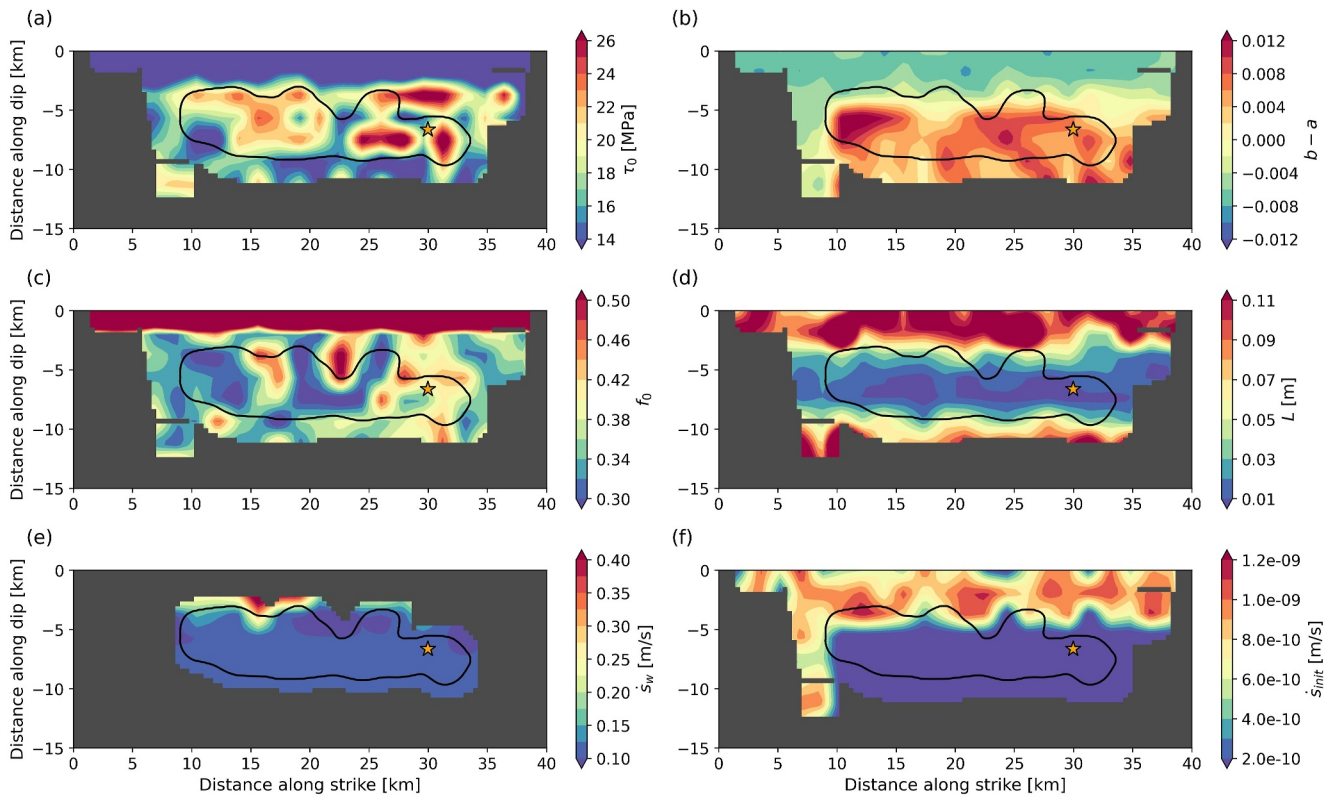


Figure 2. Dynamic parameters of the preferred joint dynamic rupture and afterslip model (preferred model) resulting from the dynamic source inversion. The parameters are bilinearly interpolated from the model grid (Figure 1d) onto the grid of the quasi-dynamic solver, which has a 400 m spacing. We consider parameters to be unconstrained in all areas of the fault where the overall fault slip (coseismic + postseismic) does not exceed 10 cm within a radius of 1.2 km. For the weakening slip rate δ_w , we only consider coseismic slip, as locally larger δ_w values do not directly affect the afterslip evolution because postseismic slip rates are generally smaller than δ_w . We do not show dynamic parameters on these unconstrained fault grid points. The black line indicates the extent of the coseismic rupture, and the star marks the hypocenter of the mainshock. (a) Prestress τ_0 . (b) Difference between the state evolution and the direct effect parameter, $b - a$. (c) Reference friction f_0 . (d) Characteristic slip distance L . (e) Weakening slip rate δ_w . (f) Initial slip rate δ_{init} (10^{-9} m/s \approx 31.56 mm/yr).

the non-constant values of Barbot et al. (2012)'s dynamic seismic cycle model, which can be approximated by $b - a = 0.004$ within the coseismic rupture area and $b - a = -0.004$ within the VS regions. The range of $b - a$ within the shallow VS region agrees with the values obtained from a dynamic afterslip inversion (Chang et al., 2013).

3.2.1.2. Reference Friction and Characteristic Slip Distance

The spatial average reference friction within the coseismic rupture area is 0.358, and its standard deviation is 0.049. The average coseismic reference friction clearly increases compared to the IM (0.313) but is still small. The average reference friction increases considerably to 0.464 when including the afterslip regions. However, this value is strongly affected by the high reference friction coefficients at the free surface.

The average characteristic slip distance L within the coseismic rupture area is 0.030 m with a standard deviation of 0.024 m, corresponding to a coefficient of variation (CV; the ratio of standard deviation to average value) of $CV = 0.80$. The average and the standard deviation increase to values of 0.057 and 0.045 m, respectively, when including the afterslip regions. L noticeably increases above and beneath the top and bottom rupture edges, respectively.

3.2.1.3. Weakening and Initial Slip Rates

The weakening slip rate δ_w and the initial slip rate δ_{init} are allowed to vary only within VS regions (Section 2.3). The δ_{init} distribution shows that the shallow afterslip regions mostly creep at a slip rate of 10^{-9} m/s (31.56 mm/yr), which is close to the plate rate. In the shallow afterslip regions, δ_w increases to values larger than 0.2 m/s. These

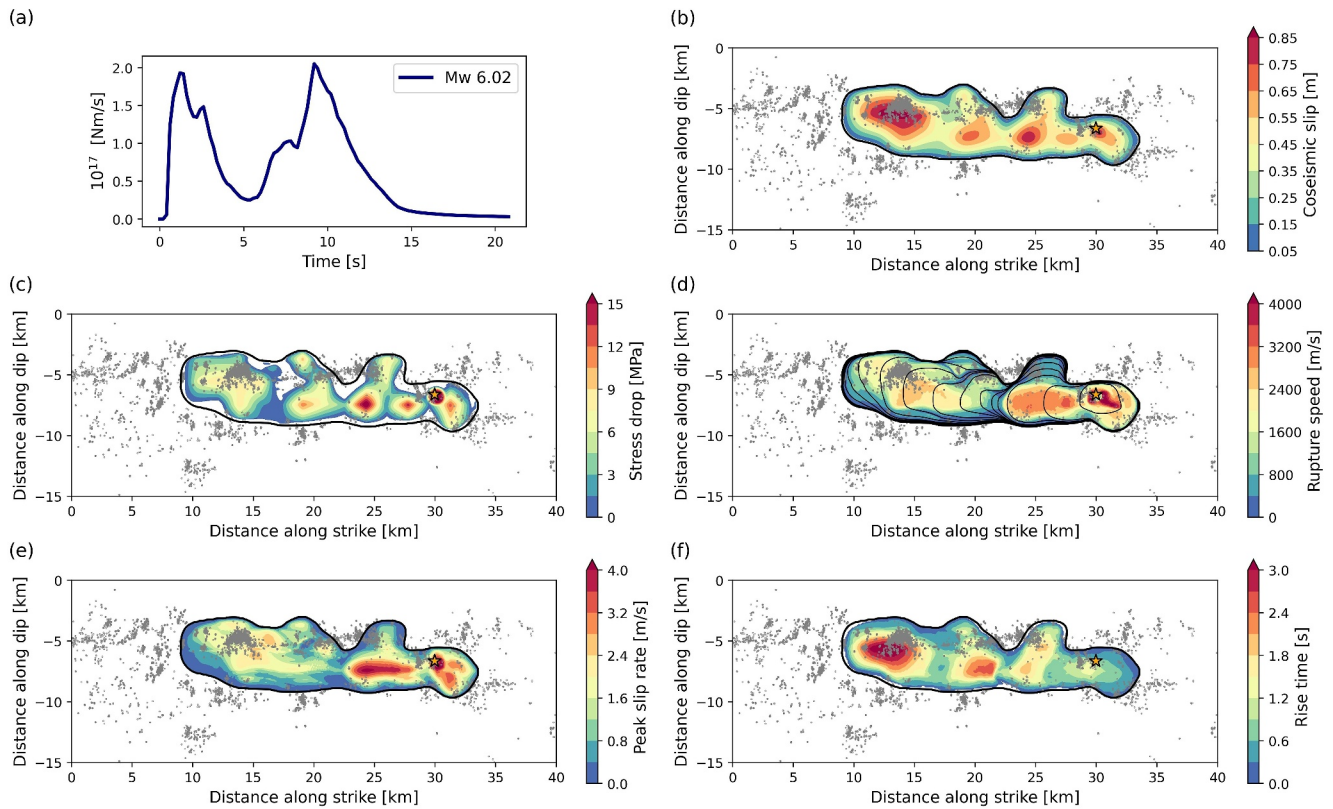


Figure 3. Coseismic dynamic rupture parameters of the preferred model. Gray dots show 90-day aftershock locations (Neves et al., 2022) projected on the planar fault plane, the black contour indicates the coseismic rupture extent, and the star marks the hypocenter. (a) Moment release rate and moment magnitude. (b) Coseismic slip. (c) Stress drop. (d) Local rupture speed and rupture front contours every 1 s. (e) Peak slip rate. (f) Rise time.

larger \dot{s}_w values do not directly affect the afterslip evolution because postseismic slip rates are generally smaller than \dot{s}_w .

3.2.2. Coseismic Rupture Dynamics

The spatially variable coseismic dynamic rupture characteristics of the PM are shown in Figure 3, together with 90-day aftershock locations (Neves et al., 2022). The PM is more complex than the IM described above. In Movie S1, we provide an animation of the PM's coseismic slip rate evolution to illustrate this complexity. Coseismic rupture separates into two distinct phases set apart by strong deceleration and acceleration of the rupture front. The minimum rupture speed occurs at 5 s rupture time. The PM concentrates slip within several asperities of varying sizes. The first phase of dynamic rupture propagation involves several smaller asperities in the vicinity of the hypocenter. The largest asperity is located in the northwestern part of the fault and ruptures during the second phase. In the northwest, rupture arrest is collocated with where the creeping section of the SAF is inferred to begin. Dynamic rupture is inferred to be pulse-like with high peak slip rates and low rise times during the first phase and transitions to crack-like with lower peak slip rates and high rise times within the large northwestern asperity. The transition from pulse-like to crack-like rupture occurs as the rupture propagates to the northwest, toward the creeping section of the SAF. We detail our definition of pulse- and crack-like rupture styles based on the ratio of rise time to rupture duration in the Supplementary Information (Text S3 in Supporting Information S1) (Heaton, 1990).

3.2.2.1. Seismic Moment Release and Coseismic Slip

Figure 3a shows the moment rate function that consists of two sharply separated peaks with a local minimum at 5 s representing the two phases of the rupture. The on-fault measured moment magnitude of M_w 6.02 corresponds to a

seismic moment of $M_0 = 1.33 \times 10^{18}$ Nm, which slightly exceeds the kinematically inferred values that fall between $1.05\text{--}1.21 \times 10^{18}$ Nm (Custódio et al., 2009; Liu et al., 2006; Twardzik et al., 2012).

The coseismic slip is confined to depths of 4–9 km and extends 3 km in the southeast direction and 20 km in the northwest direction from the hypocenter. The model's average coseismic slip is 39 cm, and the highest values reach approximately 80 cm at several small asperities close to the hypocenter and within the largest asperity 14–19 km northwest of the hypocenter. Rupture extent and asperity locations agree well with previous results from kinematic inversions (Custódio et al., 2009; Twardzik et al., 2012).

3.2.2.2. Stress Drop and Rupture Velocity

The modeled stress drop is spatially highly variable and locally takes negative values. It reaches a local maximum of 21.5 MPa, and its average is 2.7 MPa, which is similar to Ma et al. (2008)'s dynamic rupture model but lower than the value of 4.2 MPa inferred from the lowest misfit model by Twardzik et al. (2014). The highest stress drop values are reached at the asperities close to the hypocenter. Stress drops within the large northwestern asperity do not exceed 9 MPa. 7.9% of the coseismic rupture area exhibits a negative stress drop.

The fault-local rupture velocity shown in Figure 3d is highly variable. The average local rupture velocity of the PM is 1.4 km/s. This value is the spatial average of rupture speed at each grid point that coseismically slips more than 1 cm and is not equivalent to the average rupture velocity of 1.8 km/s measured from the hypocenter to the northern rupture extent. During the first second of dynamic rupture propagation, it reaches supershear velocity (Burridge et al., 1979; Das, 2015; Freund, 1979) of 4.0 km/s during the nucleation of the rupture, which is unexpectedly slow and below the Eshelby speed. While we do not account for a fault damage zone in our forward simulations, this result of the inversion may reflect the presence of a low-velocity fault zone in Parkfield (Bao et al., 2019). We discuss the challenges of accurately modeling earthquake nucleation in dynamic rupture simulations in Section 4. The PM ruptures with an average velocity of approximately 3.0 km/s to the northwest for the next 2 seconds of rupture time. After breaking through an asperity, the rupture dramatically slows down to speeds slower than 0.8 km/s between 3 and 5 s of simulation time. During the second phase, the rupture accelerates again to 2.5 km/s while breaking the large northwestern asperity. After 11 s, the rupture slows down until it arrests at 14 s after the nucleation. This slow stopping of the rupture leads to a rupture duration exceeding results from other models (Custódio et al., 2009; Ma et al., 2008; Twardzik et al., 2012).

3.2.2.3. Peak Slip Rate and Rise Time

The coseismic peak slip rate distribution correlates with the rupture speed distribution (Gabriel et al., 2013; Schmedes et al., 2010). Slip rates reach their highest values of approximately 4.0 m/s around the hypocenter but do not exceed 2.8 m/s within the large northwestern asperity. The spatial average peak slip rate is 1.3 m/s.

Coseismic rise time and peak slip rate are anti-correlated and express distinctly different rupture styles within each rupture phase. We define the coseismic rise time as the duration over which the slip rate exceeds 0.1 m/s. The rise time around the hypocenter is mostly below 1 s in accordance with results from kinematic studies (Custódio et al., 2009; Liu et al., 2006). Rise time is much larger in the northwestern asperity, where it exceeds 3 s.

3.2.3. Seismic and Geodetic Verification of Coseismic Rupture Dynamics

Figure 4 shows observed and synthetic seismic waveforms of the PM at the 30 near-field strong-motion stations used to constrain the inversion (Section 2.2). We show the maximum variance reduction at each station after cross-correlation. However, during the inversion, misfits are calculated without time shifts. The overall variance reduction, calculated from each available seismic data point, is 0.42. We generally fit the onset of the observed seismic waveforms well. The individual stations' variance reductions vary greatly. Station FZ7 exhibits the best individual variance reduction of 0.64. Station FZ11, located nearby, has the worst fit with a strongly negative variance reduction. In general, we cannot identify a clear spatial pattern in the seismic variance reduction (see Figure S7 in Supporting Information S1), except that the three stations closest to the hypocenter, where the modeled dynamic rupture is initiating due to overstress, have a less-than-average variance reduction between -0.09 and 0.18 . This suggests that local effects may dominantly cause the misfits away from the hypocenter, for example, site effects or the fault damage zone with highly variable

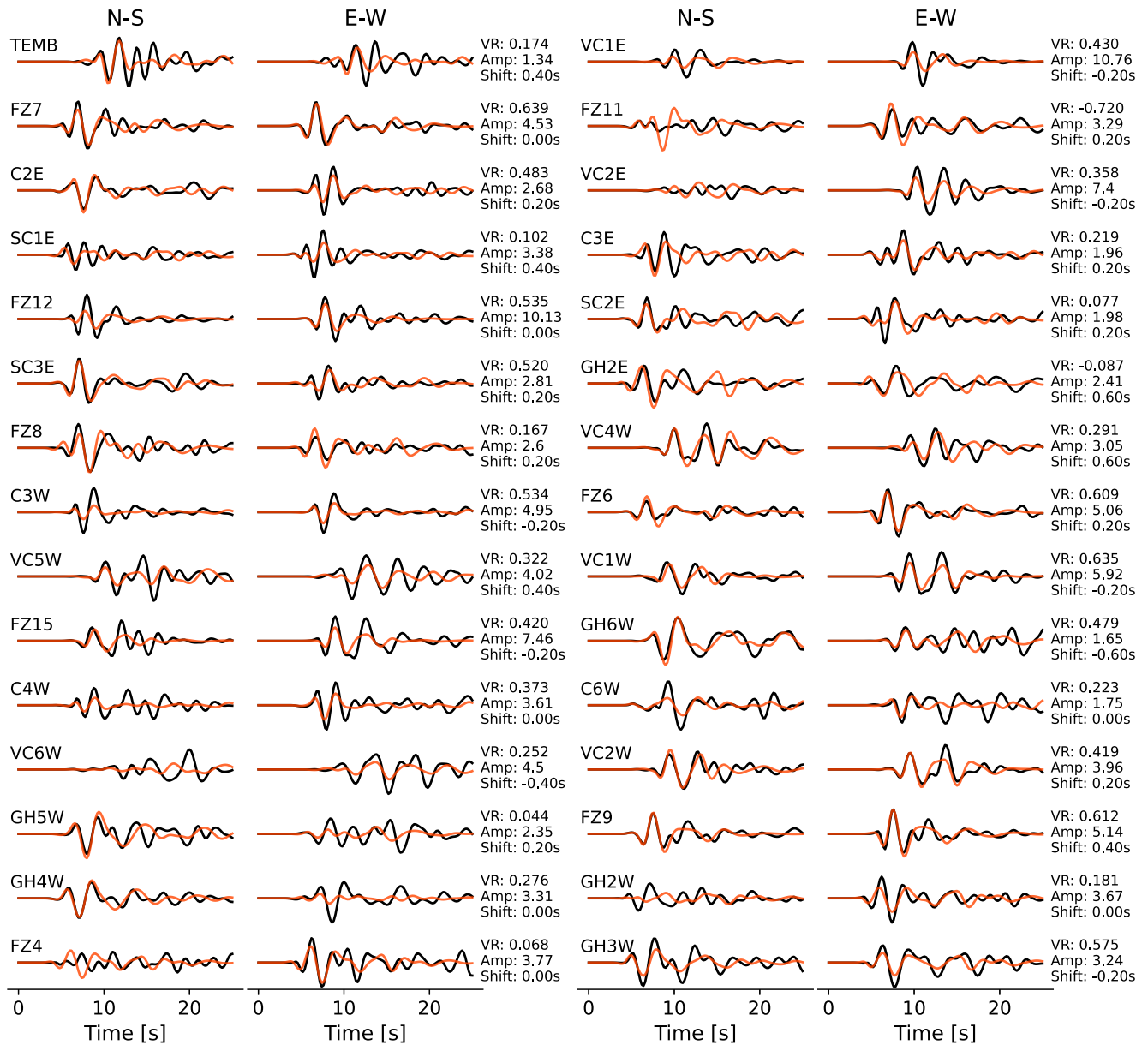


Figure 4. Observed (black) and synthetic (orange) seismic velocity waveforms from the preferred model, bandpass filtered between 0.16 and 0.5 Hz at the 30 stations used to constrain the inversion. Each waveform (synthetic and observed) is normalized by the respective station's maximum amplitude (Amp, in cm/s, either synthetic or observed maximum). In this Figure, the observed waveforms at each station are cross-correlated and time-shifted relative to the synthetics to maximize the variance reduction (VR) and to account for unmodeled effects of topography and the 3D velocity structure.

characteristics along-strike (Lewis & Ben-Zion, 2010). We note that even kinematic source inversions using the same frequency bandwidth struggle to achieve a high seismic variance reduction (e.g., Kim & Dreger, 2008).

Figure 5a shows the observed and synthetic coseismic static horizontal GPS displacements at 12 GPS stations. Synthetic and observed coseismic displacements are compared at 90 s after the rupture onset following Jiang et al. (2021a). The overall coseismic static displacement variance reduction, calculated from each available coseismic displacement data point, is 0.95, which is better than the achieved fit of a kinematic source model constrained by equally weighted seismic strong-motion and GPS data (see Figure 6b in Kim & Dreger, 2008). The modeled and observed amplitudes and directions fit nearly perfectly at most stations. Our model overpredicts the coseismic displacement at station LOWS, which is located at approximately twice the distance to the fault trace than the second farthest station.

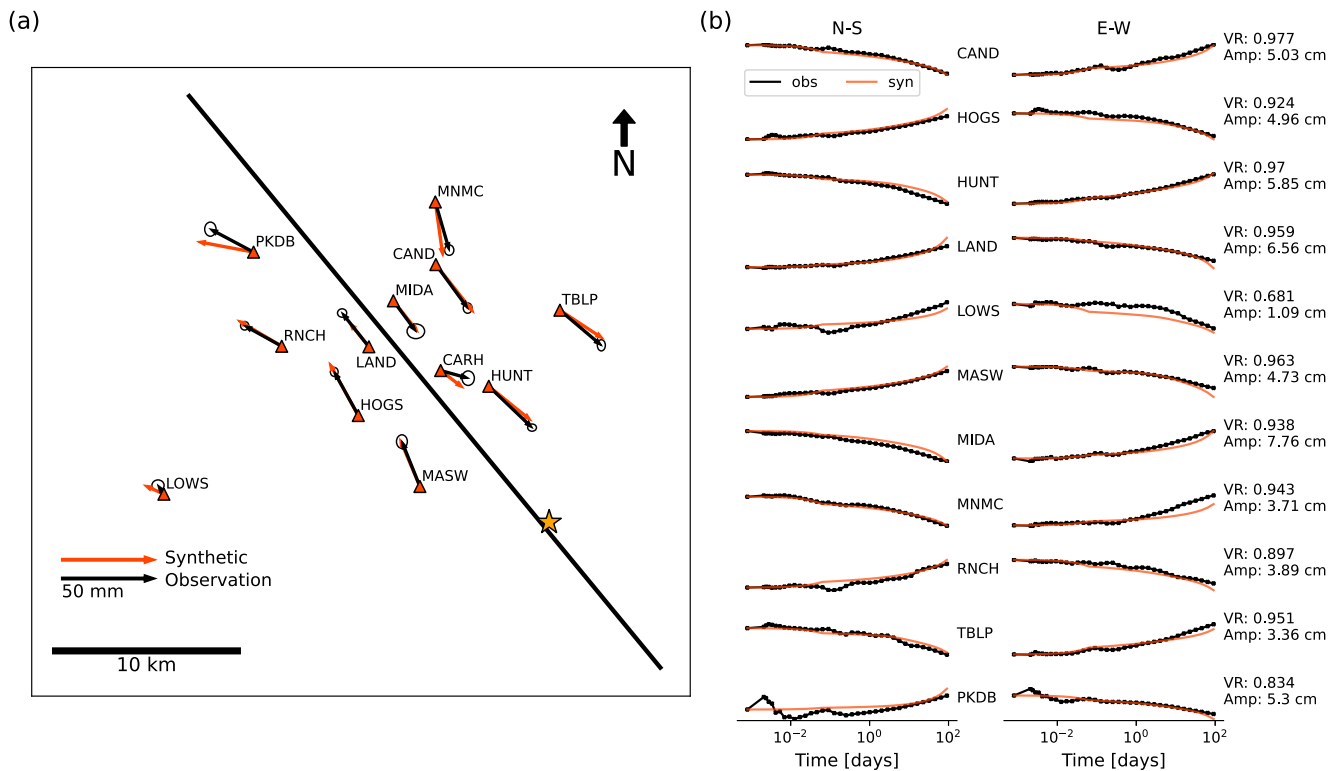


Figure 5. (a) Coseismic horizontal static displacements at 12 GPS stations. Black and orange arrows show observed (Jiang et al., 2021a) and synthetic displacements from the preferred model (PM), respectively. Black ellipses depict uncertainties of the observations. The black line indicates the model's fault trace and the star marks the epicenter. Both synthetic and observed coseismic displacements are given at 90 s after the rupture onset. (b) Postseismic evolution of the normalized displacements at 11 GPS stations (excluding station CARH) during the first 90 days following the earthquake. Black curves show observations (Jiang et al., 2021a), and orange curves show the synthetics of the PM. The time scale is logarithmic. For each station, we annotate its variance reduction inferred after removing the coseismic displacement and its maximum amplitude.

3.2.4. Geodetic Verification of Postseismic Faulting Dynamics

Figure 5b shows the normalized time evolution of the observed and modeled postseismic horizontal displacements at 11 GPS stations that constrain the 90 days of modeled afterslip. At all 11 GPS stations, largely steadily increasing postseismic displacements reach between 1 and 8 cm on each horizontal component after 90 days. All components show similar logarithmic decay rates.

The PM of our joint dynamic rupture and afterslip inversion captures the first 90 days of observed postseismic GPS deformation well. It achieves an overall variance reduction of 0.94 calculated from each available postseismic data point, which is remarkable for a dynamically consistent joint dynamic rupture and afterslip model. Similarly to the coseismic displacement misfits, station LOWS has the lowest variance reduction of 0.69. However, its contribution to the overall variance reduction is small due to the small absolute displacement amplitudes at this large distance to the fault. In particular, station PKDB shows spurious oscillations during the first minutes and hours after the earthquake, which probably reflects observational artifacts from an anomalous period of the entire network (Jiang et al., 2021a). We use a logarithmic time scale to accurately sample the early postseismic phase when computing the misfits during the inversion. This leads to a lower implicit weighting of the model's last weeks. For example, we observe a late acceleration of postseismic slip evolution at stations LAND, MASW, and PKDB 50 days after the earthquake in our model but not in observations, which likely reflects this weaker penalty. The GPS stations used in our inversion are expected to resolve shallow slip above the coseismic rupture area accurately. However, their resolution is low at depths larger than 7 km and areas located outside of the lateral extent of the coseismic rupture zone (Barbot et al., 2009; Page et al., 2009).

Figure 6a shows the postseismic slip distribution which our PM accumulates during the modeled 90 days of afterslip. The inferred afterslip is mainly confined between the free surface and the coseismic rupture area at 0–5 km

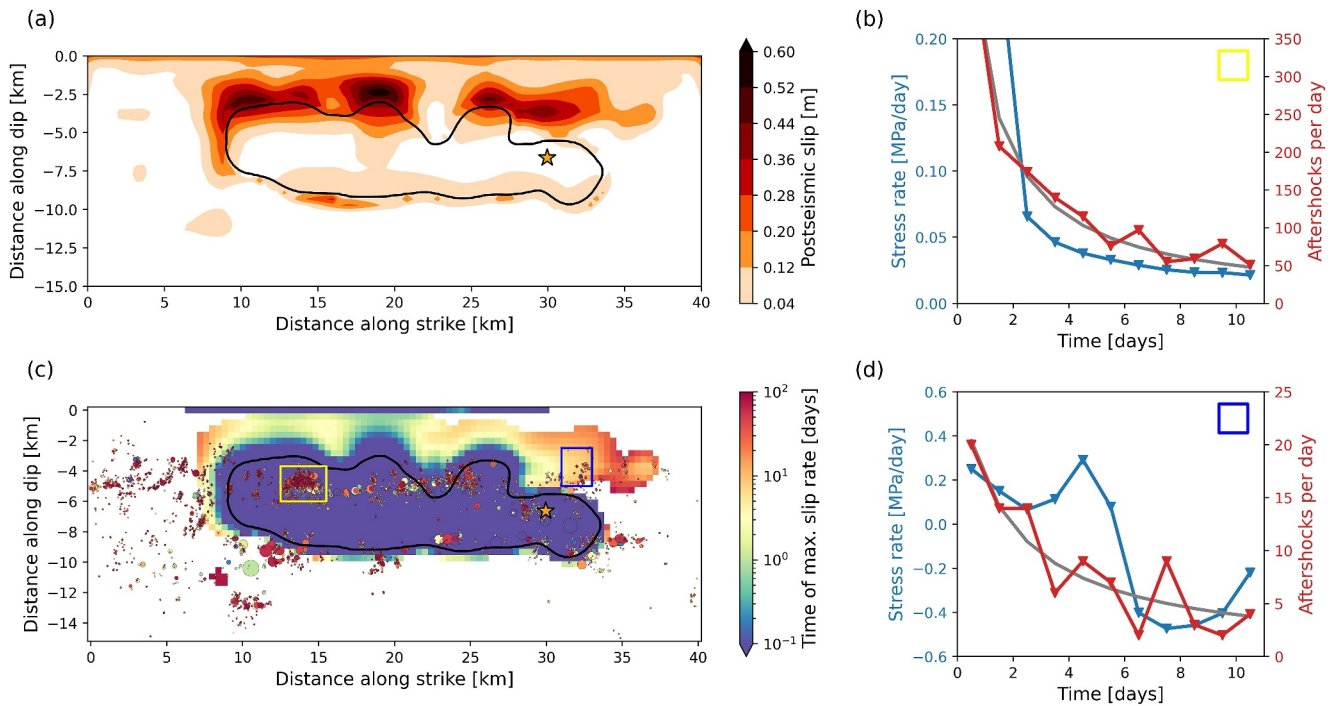


Figure 6. (a) 90-day postseismic slip of the preferred model (PM). The black contour shows the extent of the coseismic rupture, and the star marks the hypocenter. (b) Aftershock rates (red) compared to average stress rates (blue) of our PM within the yellow aftershock clusters marked in panel (c). The gray curve shows Omori's law ($n(t) = \frac{k}{c+t}$) fitted to the aftershock rates with $c = 0.68$ days and $k = 534.4$, where n represents the daily frequency of aftershocks depending on the time t since the mainshock. We selected the y-scales to emphasize the similar relative decay rates after 2 days. The apparent delay in the stress rate with respect to the aftershock rate between 1.5 and 2.5 days is just an artifact of this scaling choice. (c) Time evolution of the postseismic rupture front defined as the time of the maximum postseismic slip rate of each point where the maximum slip rate is higher than 10^{-8} m/s. The plate rate is approximately 10^{-9} m/s (Lisowski et al., 1991). Aftershock locations (Neves et al., 2022) are annotated and colored by the same logarithmic color scale, and their size is proportional to their seismic moment. The yellow and dark blue rectangles outline two aftershock clusters for which we compare aftershock rates and mean stress rates in panels (b) and (d). (d) Same as (b) for the aftershock cluster located within the dark blue rectangle marked in (c). Omori's law is fitted using $c = 1.78$ days and $k = 46.51$.

depth. Postseismic slip reaches maximum values of 50–60 cm within several slip patches, which is comparable to the maximum coseismic slip. Our model's surface offsets reach 11–17 cm after 60 days, which agrees well with surface offsets ranging from 12 to 20 cm measured on alignment arrays (Lienkaemper et al., 2006). Considerable parts of the fault that slipped coseismically continue to host afterslip. Dynamic rupture entering VS regions that host afterslip is a well-resolved and persistent feature of our model ensemble. Afterslip can reach up to 35 cm within areas that slipped coseismically, which is almost half of the maximal inferred coseismic slip. Overall, the postseismic slip evolution reflects a smooth transition from the co- to the postseismic phase supported by employing the same friction law.

A striking feature of the model's afterslip distribution is a pronounced gap in the afterslip located directly above the coseismic rupture area approximately 7–8 km northwest of the hypocenter. Such a local lack of slip is also present in the postseismic slip model of Murray and Langbein (2006). In our PM, the same area that features a gap in the afterslip acts as a strong barrier to the coseismic dynamic rupture propagation and causes strong rupture deceleration starting at 3 s after the nucleation (Figure 3b). This may reflect geologic heterogeneity along this transitional segment of the SAF. As mentioned before, the minimum coseismic rupture speed is reached at 5 s propagation time.

3.2.5. Kinematics of Afterslip and Aftershocks

Figure 6c shows the temporal evolution of the maximum postseismic slip rate and 90-day aftershock activity following the earthquake (Neves et al., 2022). During the first 3 hours after the earthquake, an afterslip front develops at the shallow perimeter of the coseismic rupture and migrates up to 2 km above the coseismic slip. Surface afterslip, possibly aided by locally low confining stress in our forward models, also initiates during the

first 2 hours after the earthquake (Langbein et al., 2005) but is initially not connected to the afterslip front migrating away from the coseismic rupture area. The fastest afterslip front is located 12 km northwest of the hypocenter and reaches the surface approximately one day after the earthquake. All major afterslip patches reach their maximum slip rate during the first 10 days following the mainshock. A small afterslip patch southeast of the hypocenter spontaneously emerges 10 days after the event and later connects to an afterslip front originating from the coseismic rupture area. The maximum modeled slip rate within this emerging afterslip patch reaches 10^{-6} m/s. However, the afterslip inferred at the southeastern part of the fault has a higher uncertainty as the sensitivity of the GPS network is lower (see Section 3.3.1 and Barbot et al., 2009; Page et al., 2009). Despite the dynamic complexity of afterslip evolution governed by rate-and-state friction, the overall mean postseismic slip rate steadily decays after 10 s (Figure S8 in Supporting Information S1).

Aftershock locations are related to the coseismic slip distribution. At the bottom and the lateral sides of the coseismic rupture area, aftershocks are mostly located at the edge or outside of the coseismic rupture area. A band of aftershocks, including the most active clusters, occurs mostly within the coseismic rupture zone between 4 and 6 km depth. Below 6 km depth, the coseismic rupture area is widely depleted of aftershocks reflecting coseismic stress release.

To analyze the spatiotemporal relationship between afterslip and aftershocks, we compare afterslip stressing rates and aftershock seismicity evolution with time. Figures 6b and 6d show aftershock rates of two aftershock clusters during the first 10 days after the mainshock. The aftershock rate of the largest aftershock cluster (yellow rectangle) compares well to our model's mean stressing rate within the cluster region. The decay of the aftershock rate n with time since the mainshock t follows Omori's law ($n(t) = \frac{k}{c+t}$, gray curve in Figure 6b) with $c = 0.68$ days. The inferred c value in this area falls within the typical range of 0–1 day and is often associated with incomplete detection of small events (Kagan & Houston, 2005; Utsu et al., 1995).

Aftershocks located within the blue rectangle in Figure 6c may be driven by an afterslip front that arrives 5–6 days after the mainshock. This afterslip front originates 4 km northwest from the hypocenter and propagates backward in the southeast direction. The average stressing rate within this region shows considerable complexity due to the passage of the afterslip front (Figure 6d). The average stress rate decreases during the first days after the mainshock. However, after 3 days, it starts to increase again, peaking at 4.5 days, which is aligned with the arrival of the afterslip stress front. Then, the stress rate rapidly decreases and turns negative due to the stress release caused by the passing afterslip. This may explain the observed considerable aftershock increase 7.5 days after the mainshock, which coincides with the maximum negative stress rate in our model. It is difficult to apply Omori's law to this aftershock cluster. To match the aftershock rate peak at 7.5 days, an unusually large c value of 1.78 days is required. Removing the peak reduces c to 1.54 days, which is yet larger than typical values. We note that afterslip in this region remains present in the mean of our best-fitting model ensemble but with increased uncertainty (see Section 3.3.1). The cumulative aftershock moments in the yellow and blue regions correspond to 4% and less than 0.1% of the PM's moment released by afterslip in the same regions and period, respectively. These values are likely too small to considerably affect observed surface displacements or to support the argument that aftershocks may drive afterslip (Barbot et al., 2009).

Figure 7a shows the afterslip rise times of the PM, which vary by more than two orders of magnitude. Within the coseismic rupture area, afterslip rise times are short and range between a few hours to a few days. Outside the coseismic rupture area, afterslip rise times rapidly increase to weeks and months. This increase gradually occurs over a distance of approximately 2 km away from the edge of coseismic rupture.

An interesting exception is a localized, approximately 4 km wide region above the hypocenter, where afterslip rise time remains constant between 15 and 20 days. Afterslip in this epicentral region originates from 4 km northwest along-strike from the hypocenter. There, coseismic rupture penetrates the shallow VS zone and initiates an afterslip front that propagates with constant rise time in the backward direction of coseismic rupture. This afterslip front propagates at a speed of approximately one km per day, which is comparable to rupture velocities of slow slip events (e.g., Vavra et al., 2023). This afterslip front may drive aftershock activity (Figure 6c and Movie S2).

The afterslip in our rate-and-state framework takes the form of different rupture styles resembling coseismic pulse-like and crack-like rupture across the same fault. The red curve in Figure 7b shows a pulse-like afterslip slip rate function associated with the afterslip region within the red rectangle in Figure 7c, where the backward propagating afterslip front is located. The average slip rate function of the adjacent region marked with a blue

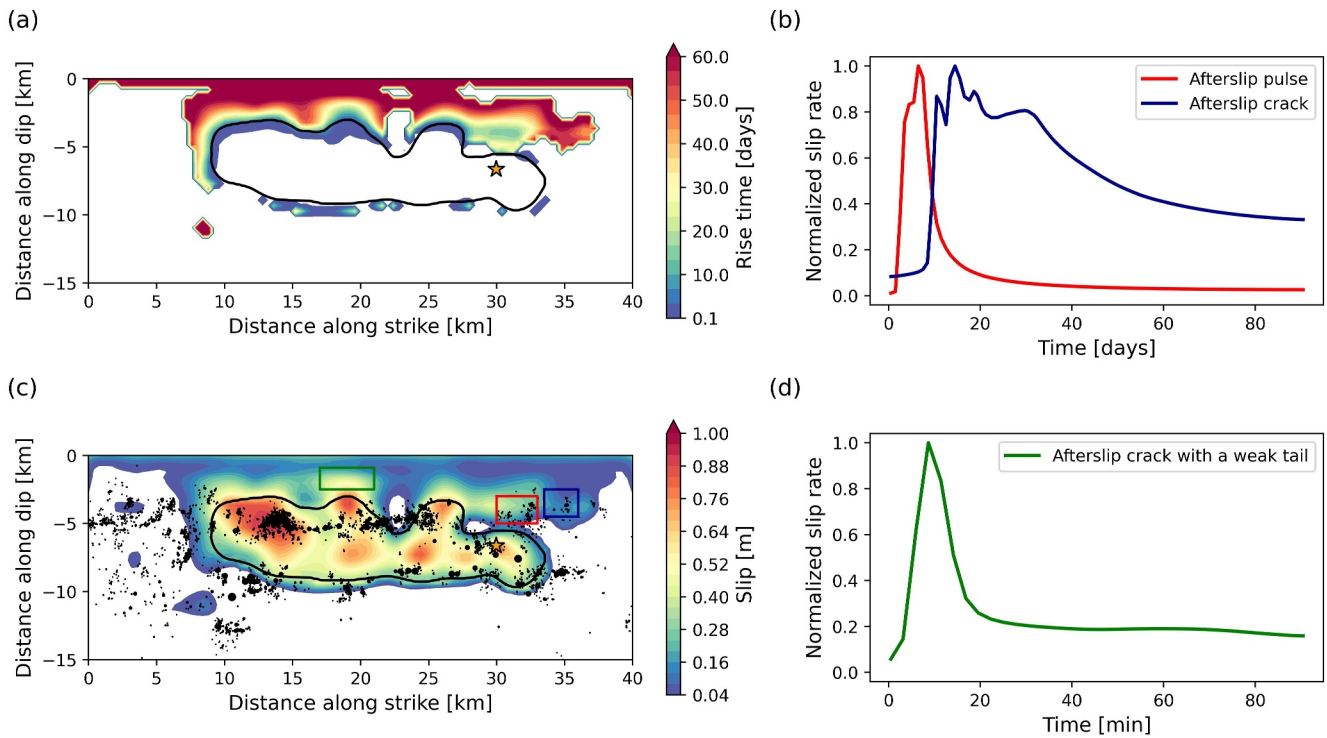


Figure 7. (a) Afterslip rise times defined as the time it takes to reach 80% of the final slip. (b) Normalized average slip rates within the red and blue rectangle marked in panel (c). (c) Combined coseismic slip and 90 days of postseismic slip of the preferred model. Colored rectangles indicate regions for which mean slip rates are shown in subplots (b) and (d). The black line indicates the extent of the coseismic rupture, black dots show aftershock locations, and the star marks the hypocenter. (d) Normalized average slip rate within the green rectangle marked in panel (c). The analyzed regions in panels (b) and (d) are not located within the coseismic rupture area, which results in the observed slip rate accelerations as the afterslip front reaches these regions.

rectangle (blue curve in Figure 7b) reveals a distinctly different slip rate behavior. Here, the slip rate function resembles a crack-like style of afterslip, remaining above 35% of the peak slip rate until the end of the 90-day simulation time. This region represents a coalescence of two afterslip fronts, the first arriving from the north-west region marked in red and the second originating from the spontaneously emerging afterslip patch to the southeast. However, the latter feature is associated with considerable uncertainties (see Section 3.3.1) and falls within the low GPS sensitivity fault region.

The green curve associated with the fault segment marked by a green rectangle (Figures 7c and 7d) shows the normalized mean slip rate function of the area with the maximum afterslip. The time scale of the afterslip in the region marked in green (minutes) differs from the time scales of the afterslip in the regions marked in red and blue (days). The associated time scales rapidly increase with distance to the extent of the coseismic rupture. This slip rate function resembles an intermediate afterslip style falling in between a pulse-like and crack-like characteristic. It is characterized by a sharper peak in the beginning and a weaker tail remaining at approximately 20% of the peak slip rate.

3.2.6. Strength Excess and Fracture Energy

Figure 8 shows the initial strength excess ($\sigma_n f_0 - \tau_0$) and the coseismic fracture energy distribution of our PM. We calculate the strength excess using the reference friction coefficient f_0 to approximate the static fault strength (see Section 4.4). However, the maximum friction coefficient reached during rupture is not a fixed, prescribed parameter of our forward model. In our simulations, the reference friction coefficient represents a lower bound of static friction within the VW regions (Ulrich et al., 2019). The strength excess distribution implies two fundamentally different coseismic rupture-stopping mechanisms. The strength excess within the coseismic rupture area is generally low, with a spatial average of 1.05 MPa. It contains negative values. Shallow coseismic rupture is partly terminated at local fault strength “barriers,” marked with blue lines in Figure 8a, which are areas with larger

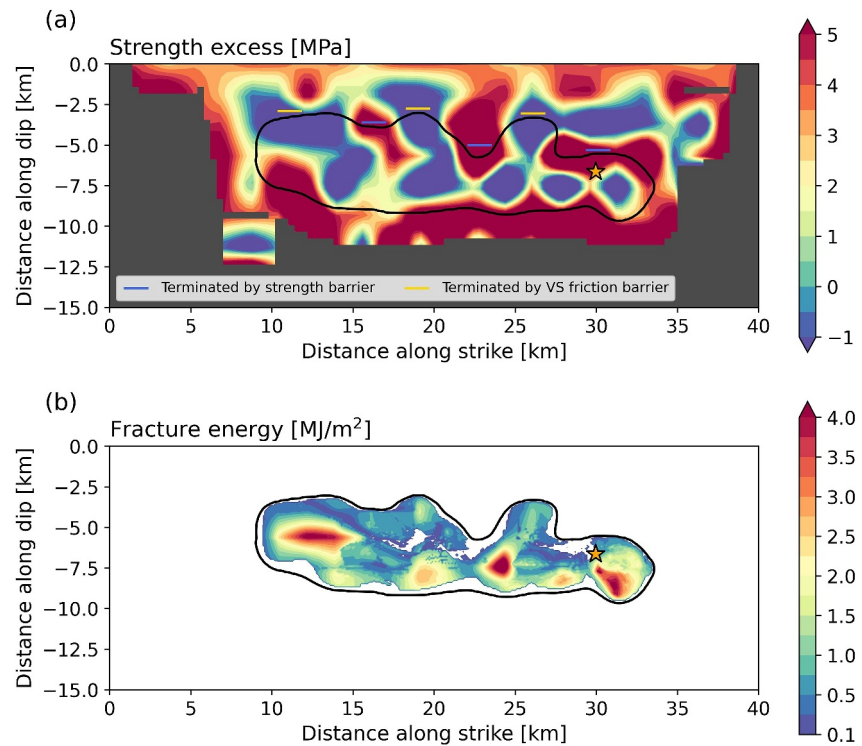


Figure 8. PM's (a) initial strength excess ($\sigma_n f_0 - \tau_0$), (b) coseismic fracture energy distributions. We only show the strength excess where coseismic and postseismic slip combined exceed 10 cm somewhere within a radius of 1.2 km, which we consider as constrained by the inversion.

strength excess than their surroundings (Pulido & Dalguer, 2009). In distinction, coseismic rupture stops in regions with negative strength excess at three shallow locations (yellow lines in Figure 8a).

We find that fracture energy is correlated with stress drop distribution (Figure 3c). We define fracture energy per unit area as:

$$G = \int_0^{x_{\min}} [\tau(x) - \tau_{\min}] dx, \quad (1)$$

where τ is shear stress, x is slip, τ_{\min} is minimum shear stress, and x_{\min} is slip at the minimum shear stress. The three regions with the largest fracture energy are located (a) southeast below the hypocenter, (b) 7 km northwest of the hypocenter, where dynamic rupture decelerates abruptly, and (c) within the large asperity 15 km northwest of the hypocenter. The spatial average of the fracture energy within the coseismic rupture area is 0.95 MJ/m^2 . Our inference here is similar to the 1.1 MJ/m^2 inferred for the similarly sized 2016 M_w 6.2 Amatrice normal faulting event (Galovič et al., 2019b). A smaller value of 0.044 MJ/m^2 has been recently inferred from earlier 3D dynamic rupture models of a sequence of small (M_w 1.9) repeating earthquakes on the SAF 25 km northwest to the 2004 Parkfield hypocenter (Gabriel et al., 2024; Lui & Lapusta, 2018), in line with the observed fracture energy scaling with earthquake - or rupture - size (Cocco et al., 2023; Gabriel et al., 2024).

3.3. Model Ensemble Characteristics and Dynamic Parameter Trade-Offs

To assess model uncertainties and trade-offs, we analyze model average quantities and their variability obtained from an ensemble of best-fitting models (Section 2.4) containing 10,500 unique model parameterizations. All standard deviations are computed with respect to the mean of the best-fitting model ensemble. The ensemble average distributions of slip, rise time, afterslip, and dynamic parameters are similar to the ones of the PM. The separation into two coseismic rupture phases with different rupture styles and the locations of co- and postseismic slip asperities are stable features of the model ensemble.

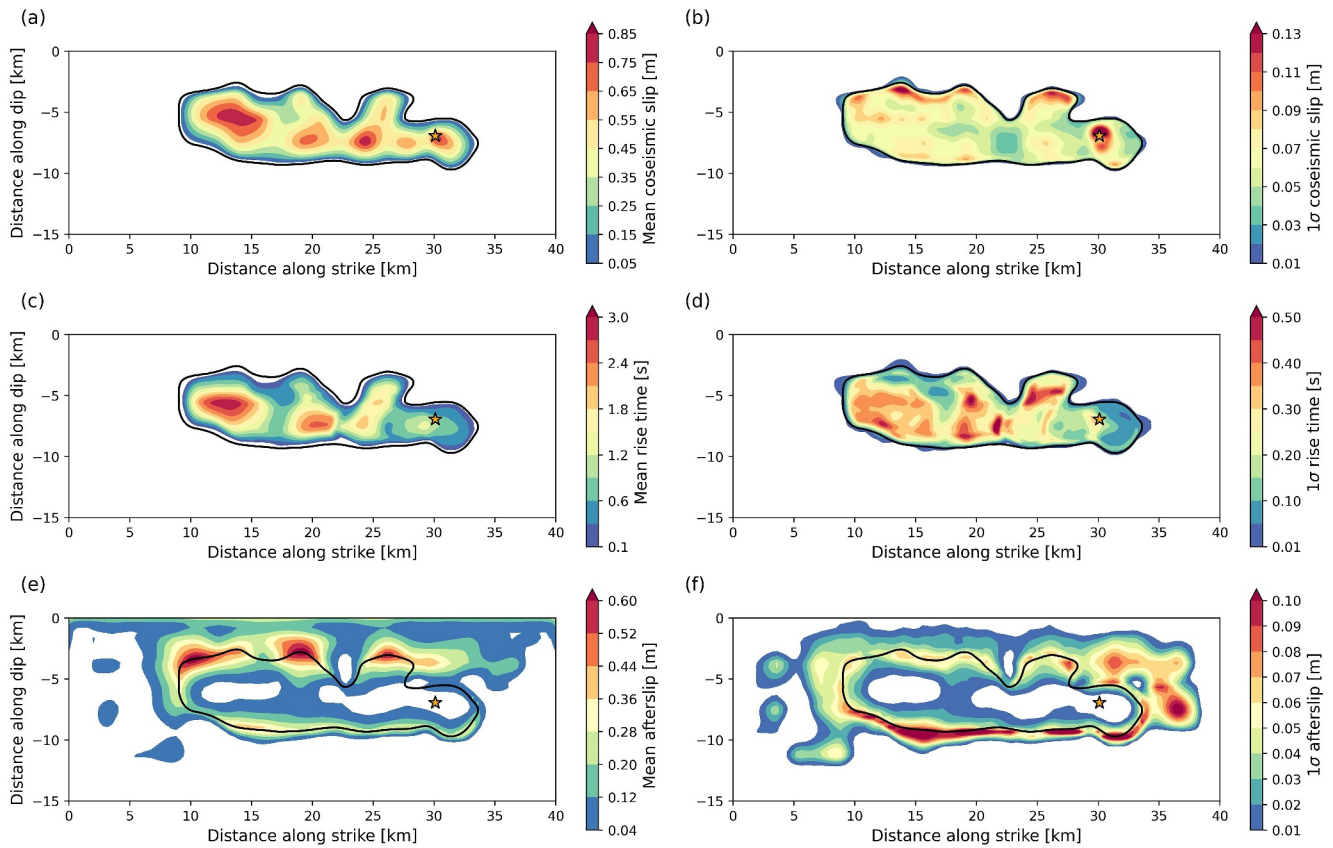


Figure 9. Ensemble average (a) coseismic slip, (c) rise time, (e) postseismic slip, and their respective standard deviations (b, d, f). Averages and standard deviations are computed from the best-fitting model ensemble containing 10,500 unique models.

3.3.1. Ensemble Averages and Uncertainties

Figure 9 shows the best-fitting model ensemble's average and standard deviation of the coseismic slip, the rise time, and the afterslip. The mean coseismic slip distribution is very similar to the slip distribution of the PM. Its spatial median coefficient of variation is 17.3%. The standard deviation distribution has its lowest values 8 km northwest of the hypocenter, where the rupture strongly decelerates. This illustrates that this rapid rupture deceleration is a critical phase of the coseismic rupture dynamics. Large standard deviation values are mostly concentrated close to the rupture edges. They reach particularly high values where the rupture terminates due to the transition to the VS regime, indicating that the abruptness of rupture termination depends on the stopping mechanism. The locally high standard deviation of the rupture contours at the same location (Figure S9 in Supporting Information S1) confirms this observation.

The mean rise time distribution shows short rise times around the hypocenter and an area with increased rise times at the northwestern end of the rupture. The coefficient of variation of both rise-time features lies in the range of 10%–20%, indicating that they are stable results of the inversion. The rise time standard deviation distribution reaches its largest value approximately 9 km northwest of the hypocenter, where the rupture accelerates again after nearly terminating.

The afterslip variability is greatest at the bottom of the coseismic rupture zone, reflecting the combined effects of varying rupture extent and the GPS network's low resolution. Another zone of high afterslip variability above and southeast of the hypocenter likely reflects the weak constraints due to the GPS network configuration, with all stations located northwest of the hypocenter. The variability is generally reduced close to the free surface, where the sensitivity of the GPS network increases.

The dynamic parameters do not vary extensively within the ensemble. Figure 10 shows the ensemble mean and the standard deviation distributions of the prestress τ_0 , $b - a$, the reference friction f_0 , and the characteristic slip

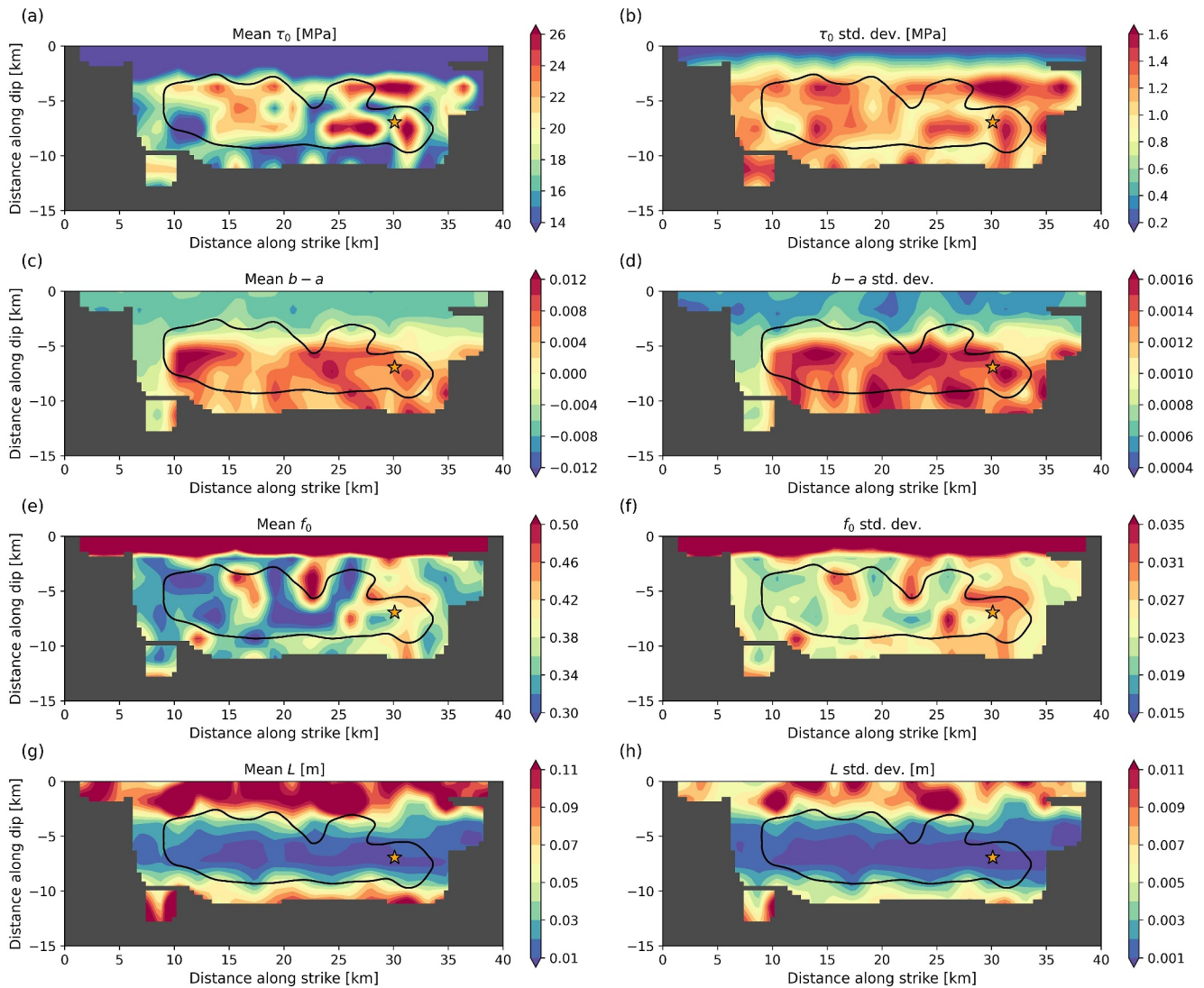


Figure 10. Mean distributions of the best-fitting model ensemble's (a) prestress τ_0 , (c) $b - a$, (e) reference friction f_0 , (g) characteristic slip distance L , and their respective standard deviations (b, d, f, h). The model ensemble contains 10,500 models. We mask areas where the sum of coseismic and postseismic slip does not exceed 10 cm within an area of a radius of 1.2 km, which we consider unconstrained.

distance L . The means of all four dynamic parameters are comparable to the PM (see Figure 2). The standard deviations are relatively small and highly correlated with the corresponding mean distributions. Plotting the coefficient of variation of the four dynamic parameters or a strictly positive equivalent (see Figure S10 in Supporting Information S1) confirms this observation. The coefficients of variation of all four parameters are spatially rather homogeneous, with values ranging mostly between 4% and 8%. Within the coseismic rupture area, τ_0 has the smallest and L the largest relative uncertainties.

3.3.2. Ensemble Correlations and Source Parameters

The prestress is locally (anti-)correlated with $b - a$ and f_0 , while overall correlation values between different dynamic parameters are small. Figure 11 shows correlation coefficients of the ensemble's dynamic parameters to analyze trade-offs between them. Correlation coefficients rarely exceed ± 0.4 . Locally, prestress τ_0 and reference friction coefficient f_0 share the highest positive correlation. Maximum values up to 0.4 are reached in areas where coseismic and postseismic slip overlap, likely because prestress variations can be dynamically balanced by changes in the reference friction coefficient. τ_0 and $b - a$ show an anticorrelation of up to -0.3 . High anticorrelation in areas with large rise times may indicate that a careful balance between τ_0 and $b - a$ is important to

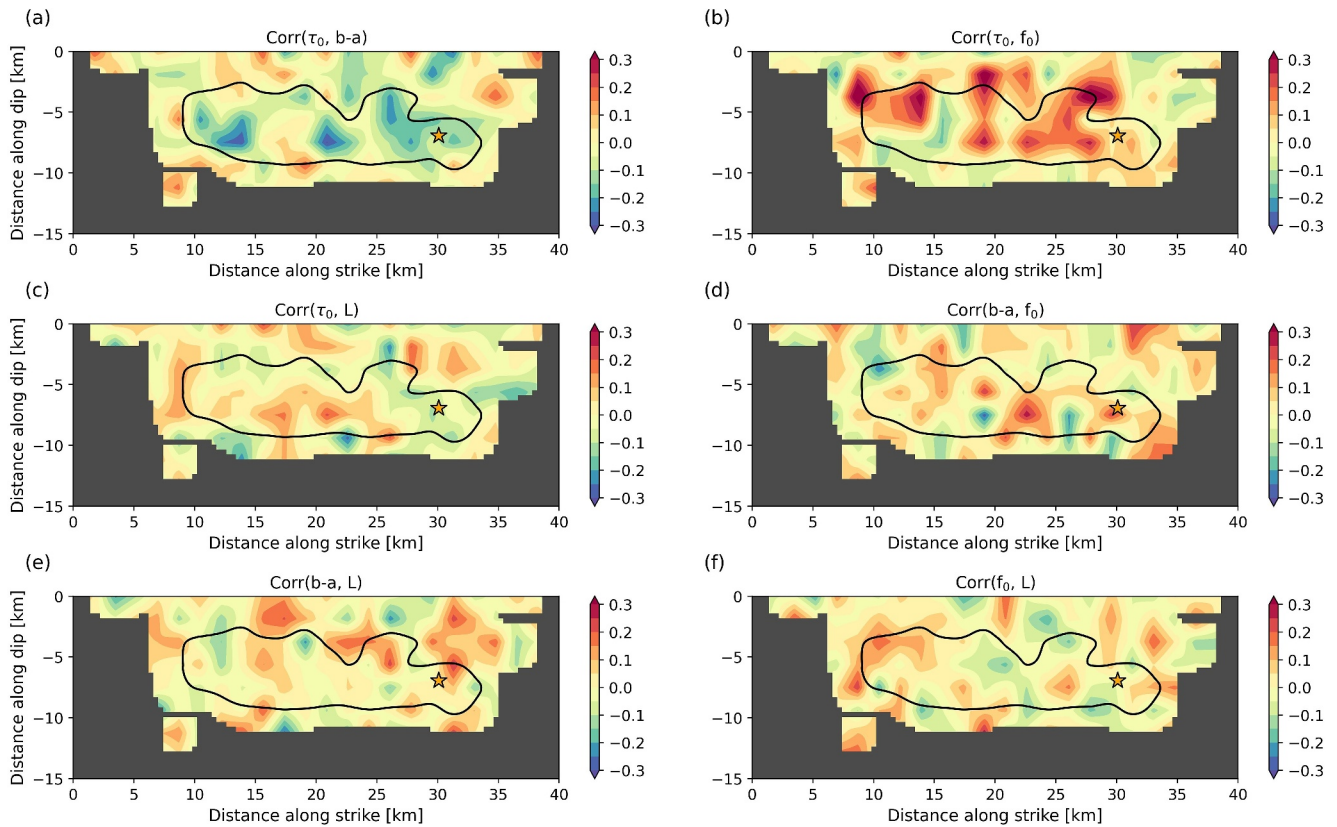


Figure 11. Ensemble correlation coefficients' spatial distribution of dynamic parameter pairs (a) τ_0 and $b - a$, (b) τ_0 and f_0 , (c) τ_0 and L , (d) $b - a$ and f_0 , (e) $b - a$ and L , (f) f_0 and L . The black contour indicates the extent of the coseismic rupture, and the star marks the hypocenter. We mask areas where the sum of coseismic and postseismic slip does not exceed 10 cm within an area of a radius of 1.2 km, which we consider unconstrained.

facilitate sustained crack-like rupture. Slip-weighted average correlation coefficients of the other four parameter pairs are below 0.02.

When considering only afterslip, still f_0 and τ_0 still exhibit the strongest correlations. Zhao and Yue (2023) showed that the afterslip evolution under steady-state assumption depends on the difference $\tau_0 - \sigma_n f_0$. Our results also indicate significant trade-offs between τ_0 and f_0 when accounting for the weakening phase. The advantage of probabilistic approaches is their ability to accommodate trade-offs and unresolved parameters. Nevertheless, the parameter space of future dynamic inversions might be minimized by jointly inverting for $\tau_0 - \sigma_n f_0$. Additionally, we find a locally high anticorrelation between δ_{init} and $b - a$ for the afterslip above the hypocenter (Figure S11 in Supporting Information S1).

The dynamic source inversion approach facilitates computing fundamental earthquake source parameters such as radiated energy and fracture energy while simultaneously relying on observed data and the underlying physics. Figure S12 in Supporting Information S1 displays histograms of various coseismic and postseismic rupture parameters of the best-fitting model ensemble. We find an ensemble average radiated energy of 2.19×10^{13} J and an average coseismic fracture energy of 8.30×10^{13} J, which translates to an average radiation efficiency of 21%.

4. Discussion

4.1. Mixed Crack- and Pulse-Like Rupture Dynamics Governed by Local Fault Heterogeneity

It remains debated whether earthquakes predominantly propagate as cracks or as pulses (Heaton, 1990). For example, Lambert et al. (2021) hypothesize that large megathrust events mainly rupture as “mild” cracks whereas crustal strike-slip faults rupture in the form of self-healing pulses. We infer a clear transition from pulse-like to crack-like (see Text S3 in Supporting Information S1) coseismic rupture of the crustal strike-slip 2004 Parkfield

earthquake. This may indicate that the style of earthquake rupture rather depends on local rheological and frictional properties than on the regional tectonic setting and that one earthquake may comprise more than one rupture style (e.g., Gabriel et al., 2012).

We analyze the spatial correlation between rise times and dynamic parameters (Figure S13 in Supporting Information S1) of our PM to understand the underlying factors causing the coseismic rupture style transition. The overall geometrical simplicity of the Parkfield segment suggests that the observed rupture behavior is driven mainly by initial stresses and specific local frictional properties. While rise time does not correlate with the prestress τ_0 (correlation coefficient $cc = -0.05$), it depends on the interplay between $f_0 - f_w$, $b - a$, and L . The reference friction drop exhibits the highest (anti-)correlation of -0.59 with rise time. The largest rise times are reached when the reference friction drop is smaller than 0.05 . L shows an anticorrelation (-0.39) with rise time and $b - a$ shows a positive correlation of 0.47 with rise time. These results imply that a VW regime, with small L and small $f_0 - f_w$, promotes crack-like rupture. The observed anticorrelation between rise time and reference friction drop is consistent with the dynamics of self-healing rupture pulses (Brune, 1970; Heaton, 1990). From theory (Perrin et al., 1995; Zheng & Rice, 1998) and previous numerical studies (e.g., Gabriel et al., 2012), we expect that for dynamically sufficiently weak faults the selection between cracks and pulses, and their coexistence, has a non-trivial dependence on initial conditions. However, healing fronts emerging from coseismic rupture termination also locally reduce rise times, as seen above the hypocenter and at the northwestern end of coseismic rupture (see Movie S1). Contrary to our results, Ampuero and Rubin (2008) report an anticorrelation between $b - a$ and rise time. Velocity-strengthening regions affect these correlations. When only considering VW parts, the correlations between rise time and $b - a$, $f_0 - f_w$, and L , change to 0.39 , -0.71 , and -0.30 , respectively. We conclude that a complex interplay of fault-local dynamic parameters determines the rupture style.

In our PM, both rupture styles produce vastly varying seismic radiation. Figure S14 in Supporting Information S1 shows a waveform comparison with synthetics generated by a 5 s version of our PM, including only the initial pulse-like phase. The short model's overall seismic variance reduction reaches 95.3% of the full model's variance reduction, but the short model cannot explain the displacements measured by the GPS stations. The initial pulse-like phase produces most of the seismic radiation while accounting only for 35.7% of the seismic moment, in agreement with observations (Allmann & Shearer, 2007).

This is consistent with our inferred gradual transition from the coseismic to the postseismic phase. Coseismic rupture dynamics initiate as a strongly radiating phase, followed by a mildly radiating phase, which only weakly imprints on the seismic data but produces dynamic perturbations in the GPS data (Jiang et al., 2021a). Finally, aseismic afterslip dominates with rise times increasing with time and distance from the coseismic rupture area (Figure 7). These results highlight the importance of complementary data sets to infer kinematic and dynamic source models and have important implications for seismic hazard assessment: Similarly sized earthquakes can cause vastly different ground motions based on the dominantly operating rupture style, and large earthquakes can experience strong local amplifications due to dynamic rupture complexity (Schliwa & Gabriel, 2023).

4.2. Rupture Duration and Rupture Speed Variability

We observe locally pronounced variations in rupture speed in the dynamic inversion, with rupture durations exceeding those inferred from many kinematic source models (e.g., Custódio et al., 2005, 2009; Liu et al., 2006). The rupture speed changes cause a bimodal moment rate function, which together with the long rupture duration are stable features of the best-fitting model ensemble (Figure S15 in Supporting Information S1). Fletcher et al. (2006) determined the rupture velocity using back-projection, identifying the last well-correlated high-frequency pulse at 4 s after nucleation, 9 km from the hypocenter. This timing aligns with the changes in rupture speed and rupture style in our dynamic inversion model (Figure S16 in Supporting Information S1). They did not find high-frequency sources at the northwestern asperity, where we observe a mildly radiating crack-like rupture, which produces only weak seismic radiation >0.16 Hz (cf. Figures S4 to S14 in Supporting Information S1). In contrast, Allmann and Shearer (2007) still found a burst of high-frequency seismic radiation originating at the southern edge of the northern high-slip patch approximately 13 km northwest of the hypocenter. Our model ensemble persistently features a strong rupture deceleration and subsequent acceleration between the southeastern and northwestern parts of the rupture. Such abrupt changes in rupture velocity can explain the observed high-frequency radiation (e.g., Madariaga, 1977; Schliwa & Gabriel, 2023; Shi & Day, 2013). Jiang et al. (2021a) observed that dynamic

displacements measured with GPS stations, which are sensitive to lower frequencies, lasted twice as long (60 s) as the shaking recorded with strong motion sensors. This may help explain the rupture duration differences between our results and many kinematic models that rely solely on accelerometer recordings with frequencies >0.16 Hz. Additionally, a study analyzing near-fault strong ground motions reported no evidence of sustained supershear rupture (Shakal et al., 2006), while some kinematic models require (near) supershear rupture speeds that produce minimal slip (Custódio et al., 2005; Liu et al., 2006).

Different studies disagree on the potential supershear onset of the 2004 Parkfield earthquake. Similar to the rupture speed in our PM, Custódio et al. (2009) reported a supershear rupture onset with velocities above 4 km/s during the first second of their kinematic source model. However, Ma et al. (2008)'s forward dynamic rupture model B does not exhibit an initial supershear rupture velocity, while Twardzik et al. (2014)'s simple two-ellipse dynamic inversion model nucleates at supershear speed (3.8 km/s), illustrating the non-uniqueness of proposed early rupture phases fitting observations with different model approaches. Dynamic rupture simulations mostly employ prescribed nucleation procedures, which can introduce additional challenges in accurately modeling rupture onset. We note that dynamically, supershear rupture may initiate at the onset of rupture, without requiring propagating a certain distance, if the fault is locally weak or highly prestressed (e.g., Gabriel et al., 2012). The above mentioned models do not feature the strong rupture deceleration after 3 s. Fletcher et al. (2006) also inferred a fast rupture onset but without reaching supershear speeds. In their study, the rupture starts with a velocity of 3.3 km/s and then drops below 1 km/s. The observed drop in rupture velocity aligns perfectly with the rupture deceleration in our PM (Figure S16 in Supporting Information S1).

The rupture speed change in our model ensemble is caused by a strong fault strength barrier (Figure S17a in Supporting Information S1) that extends from 8 to 3 km depth and also creates an afterslip gap (Figure 9e). This barrier is a well-constrained feature of our model ensemble and coincides with a low v_s area in along strike-direction imaged at 3 km depth (see Figure 6d in Zeng et al., 2016), which might represent a geological or rheological feature.

4.3. Dynamic Rupture Arrest

We find that distinct dynamic rupture-stopping mechanisms of different parts of coseismic rupture correlate with locally distinct afterslip evolution.

During dynamic rupture, elastic strain energy release competes with the consumption of fracture energy (Barras et al., 2023; Cocco et al., 2023; Ke et al., 2018). On a planar fault, dynamic rupture terminates if (i) it dynamically runs out of available strain energy; or (ii) local changes in normal stress or frictional conditions increase the required fracture energy or lead to VS conditions. At three shallow locations (yellow lines in Figure 8a), coseismic rupture stops in regions with negative strength excess. Comparing the coseismic rupture contours with the $b - a$ distribution (Figure 2b) reveals that dynamic rupture terminates at these locations because it enters VS regions. Later, these three locations form the origin of the main afterslip patches (Figure 6a). There is no or very little afterslip evolving in regions where coseismic rupture is stopped due to local strength excess barriers.

The dynamic parameters L and \dot{s}_w additionally contribute to the dynamic rupture arrest. When coseismic rupture propagates into VS parts of the fault, slip rates cannot reach the locally increased \dot{s}_w values anymore (Figure 2e), accelerating the rupture arrest. L noticeably increases above and beneath the coseismic rupture area (Figure 2d). However, rupture arrest in the along-strike direction is not associated with an increase of L .

4.4. Coseismic Stress Drop, Friction Drop and Implications for the Heat Flow Paradox

Our modeled low average coseismic stress drop may reflect the Parkfield section's comparably short recurrence times. The PM's average on-fault measured coseismic stress drop is 2.76 MPa which is rather small. We compare the on-fault dynamic stress drop to a seismological Brune-type stress drop estimate from calculating the average stress drop from the moment rate function spectrum using the following equation (e.g., Kaneko & Shearer, 2014):

$$\Delta\sigma_{ef} = \frac{7}{16} \left(\frac{f_c}{k\beta} \right)^3 M_0, \quad (2)$$

where $f_c = 0.156$ Hz is the corner frequency of a Brune spectrum (Brune, 1970) fitted to the moment rate function spectrum of the PM (Figure 3a), $\beta = 3600$ m/s the average S-wave velocity, $M_0 = 1.33 \times 10^{18}$ Nm the seismic moment, and k is a constant depending on the assumed source model. The resulting $\Delta\sigma_{ef} = 2.72$ MPa reproduces the average on-fault stress drop when assuming $k = 0.26$, which is the value for S-wave spectra of the cohesive-zone model by Kaneko and Shearer (2014). Allmann and Shearer (2009) found that moderate to large strike-slip earthquakes have a median stress drop of 10 MPa when assuming the Madariaga (1976) source model. We infer $\Delta\sigma_{ef} = 5.16$ MPa when using $k = 0.21$ from the Madariaga source model, which is approximately half of the 10 MPa median value that Allmann and Shearer (2009) inferred for moderate to large strike-slip earthquakes. The mean f_c of the 10,500 models of the best-fitting model ensemble is 0.159 ± 0.018 Hz. Zhang et al. (2022) analyzed the spatial variability of stress drops of M_w 0–4 earthquakes along the Parkfield section of the SAF. They found exceptionally high stress drops close to the 2004 Parkfield hypocenter, which aligns with the area where our dynamic models also exhibit the highest stress drops. This correlation may reflect locally persistent frictional conditions that favor higher stress drop ruptures.

The SAF is a mature fault system that is assumed to operate under relatively low absolute stress levels based on the absence of a heat flow anomaly (e.g., Lachenbruch & Sass, 1980; Rice, 1992; Williams et al., 2004) and borehole measurements at the SAF Observatory at Depth (e.g., Hickman & Zoback, 2004). The absence of a heat flow anomaly above the SAF may be explained by statically strong and dynamically weak faults due to strong dynamic weakening at coseismic slip rates or by an effectively low static fault strength with respect to Byerlee's law (Byerlee, 1978). A statically weak SAF may be caused by weak fault gouge (Lockner et al., 2011) or elevated pore fluid pressure (Rice, 1992).

Using a friction law with a rapid-weakening mechanism at coseismic slip rates allows faults to operate at low average shear stress (Noda et al., 2009; Ulrich et al., 2019). Our PM exhibits a small average reference friction drop ($f_0 - f_w$) of 0.058 within the coseismic rupture area, which would not align with the concept of statically strong and dynamically weak faults. However, the reference friction drop, is not necessarily representative of the effective friction drop. The low-velocity steady-state friction f_{LV} depends on the initial slip rate \dot{s}_{ini} , the reference slip rate \dot{s}_0 , and $b - a$ (see Equation S5 in Text S1 in Supporting Information S1). The maximum friction coefficient reached during rupture is not a prescribed model parameter but varies along the fault and often exceeds f_0 , but rarely falls below this value. We calculate the effective friction drop as $f_{max} - f_{min} = \tau_{max}/\sigma_n - \tau_{min}/\sigma_n$ and infer an average value of 0.41 within the VW regions of the coseismic rupture area of the PM. This larger effective friction drop is yet smaller than expected from Byerlee's law and a lithostatic pressure gradient.

We note that our ensemble of dynamic rupture models might be biased by the choice of the initial model (IM), which has an even smaller average reference friction drop. Although we cannot exclude that an alternative dynamic rupture model with a different reference friction drop may fit the data, the construction of the IM (Section 3.1) demonstrates that considerably larger fracture energy is likely incompatible with the earthquake's large-scale rupture properties. The comparably small average coseismic characteristic slip distance of 3 cm is approximately 25% of the expected value considering the earthquake's magnitude and rupture size (Gabriel et al., 2024; Palgunadi et al., 2024). As we cannot achieve a higher reference friction drop without a shorter characteristic slip distance while preserving fracture energy, we consider a higher friction drop dynamic model unlikely to be mechanically viable.

4.5. Negative Coseismic Stress Drop May Promote Afterslip and Aftershocks

In our PM, 7.9% of the coseismic rupture area exhibits a negative coseismic stress drop. We find that the largest connected area of negative coseismic stress drop at 12–13 km northwest to the hypocenter (Figure 3c) coincides with the area of most afterslip within the extent of the coseismic rupture (Figure 6a). Mikumo and Miyatake (1995)'s dynamic rupture model of the 1984 Morgan Hill earthquake featured negative stress drops to explain small slip over a shallow fault section, which they associated with VS behavior (Blanpied et al., 1991; Quin, 1990). Similar to Mikumo and Miyatake (1995)'s model, our results include a small average strength excess, which likely promotes negative stress drops. Using dynamic-weakening friction, Noda and Lapusta (2010) inferred regions of negative stress drop also for VW areas with slip larger than the average slip.

We observe that areas of negative stress drop align with the depth of increased aftershock activity. Custódio et al. (2009) found that aftershocks tend to occur in regions of negative stress change in a stress change model

inferred from a kinematic slip model. Here, we observe an interesting relationship between the aftershock locations and the slip distribution of our PM, which is compatible with this observation. At the bottom and the lateral edges of the coseismic rupture area, aftershocks are mostly located outside of the coseismic rupture area (Figure 6c), where a stress increase is expected (Figure S18 in Supporting Information S1). In contrast, the shallow aftershock clusters between 4 and 6 km depth occur still within the coseismic rupture zone, where a static stress change model would produce a negative stress change. In our rate-and-state friction model, shallow rupture is often stopped by VS friction. The shallow aftershocks coincide with the transition from a VW to a VS regime (Figure 2b). Our model demonstrates that this transition zone can exhibit a considerable area of negative stress drop, which is compatible with increased aftershock activity.

4.6. Correlations of Kinematic Parameters

The relationship between kinematic parameters has been analyzed in previous ensembles of dynamic rupture models (Gabriel et al., 2013; Guatteri et al., 2004; Mai et al., 2017; Oglesby & Day, 2002; Schmedes et al., 2010, 2012; Song et al., 2013; Vyas et al., 2023) and differences may depend on the local heterogeneity of dynamic parameters. Schmedes et al. (2010) generated a correlation matrix of kinematic rupture parameters from >300 heterogeneous strike-slip dynamic rupture models using linear slip-weakening or linear time-weakening friction. Consistent with their results, we find correlations greater than 0.8 between rupture speed and peak slip rate, as well as between rise time and slip for the best-fitting model ensemble (Figure S19 in Supporting Information S1). While Schmedes et al. (2010) reported weak anticorrelations between rise time and peak slip rate, and between rise time and rupture speed, our ensemble shows these as weakly positive. Vyas et al. (2023) correlated kinematic rupture parameters of dynamic rupture models with thermal pressurization and mostly homogeneous initial conditions. Contrary to our results, they find anticorrelations between peak slip rate and slip, rupture speed and slip, and rise time and peak slip rate. Despite the additional weakening effects due to thermal pressurization, we speculate that these differences stem primarily from the homogeneous initial conditions and simple rupture dynamics, which create a shared dependence on rupture propagation distance.

4.7. Limitations and Future Developments

The dynamic inversion is constrained by frequencies up to 0.5 Hz which limits the spatial and temporal resolution. However, due to the nonlinearity of the forward problem and the physics-based constraints provided by rate-and-state friction, it remains challenging to directly infer the achieved resolution from the data resolution. Nevertheless, small-scale features of our models need to be interpreted with care. We use rise time differences to differentiate between rupture styles, which appear reasonably constrained by the dynamic relations enforced by the friction law. The dynamic inversion tracks the rupture front, and thereby, constrains the rupture speed. The final model ensemble shows high rupture speeds near the hypocenter, consistent with array-based rupture front tracking (Figure S16 in Supporting Information S1, Fletcher et al., 2006) and previous kinematic models (e.g., Custódio et al., 2009; Liu et al., 2006). High rupture speed correlates with high peak slip rate in our best-fitting model ensemble, where the correlation coefficient is 0.85 (Figure S19 in Supporting Information S1). While the dynamic inversion constrains friction parameters and, consequently, radiation efficiency, resolving whether there is a weak slip rate tail (Lambert et al., 2021) using strong motion data alone is difficult. Similarly, the observational estimation of rise time remains severely challenged by the limited resolution and inherent non-uniqueness of kinematic source inversions (Gallovič & Ampuero, 2015; Ide et al., 2005; Page et al., 2011). However, in our inversion, GPS data additionally constrain the modeled slip and the rise time of an impulsive rupture with a high slip rate. This is supported by the rise time variability of the initial impulsive phase within the model ensemble, which is mostly below 0.25 s (Figure 9). We set the threshold for computing rise time relatively high (>0.1 m/s) to ensure reasonable constraints between crack- and pulse-like rupture (Text S3 in Supporting Information S1).

Our 90-day afterslip simulation does not account for viscoelastic effects. Freed (2007) suggest that the 2004 Parkfield postseismic deformation was solely caused by afterslip, and viscoelastic relaxation and poroelastic rebound had no significant contribution. In distinction, Bruhat et al. (2011) argue that viscoelastic relaxation is required to explain as much as 20% of the postseismic displacement at the GPS station farthest from the source (LOWS, see Figure 1a) 5 years after the earthquake. Based on their analysis, the contribution of viscoelastic relaxation to near-source displacements during the early postseismic time may be negligible (see Figure 8b in

Bruhat et al., 2011). There is also evidence for deep afterslip from substantial acceleration of low-frequency earthquake occurrences (Johnson et al., 2013; Shelly & Johnson, 2011), deeper than our model domain.

Despite running more than 2 million dynamic rupture forward simulations, our inversion visits only a tiny portion of the large model space associated with ≈ 1100 dynamic parameters. Our inverse problem also has a large null space (model parameters not affecting the misfit) because wide parts of the fault do not slip significantly, which can be realized by a wide range of model parameters. By providing a reasonable IM and guiding the inversion during the convergence phase by occasionally selecting our PM and restarting all Markov chains with the chosen model, we were able to find an ensemble of models that explains the coseismic and postseismic data, which is a similar approach to previous studies (Galović et al., 2019b; Premus et al., 2022). However, our best-fitting model ensemble cannot be assumed to be completely independent of the IM. In particular, many parameter combinations can facilitate dynamic rupture arrest without being constrained by subsequent afterslip. Parameters in these regions have high uncertainties, low impact on the misfit, and may still depend on the IM. While the model uncertainties we provide represent ranges of parameters that can fit the data, we cannot expect the uncertainty quantification to be mathematically complete in a Bayesian probabilistic sense.

The overall similarity between models within the ensemble may bias the absolute correlation coefficients. We find that the correlations between the different dynamic parameters of the ensemble (Figure 11) are generally low (<0.5). However, the correlation coefficients of the best-fitting model ensemble increase with the length of the Markov chains and might rise further when the inversion is continued. Longer Markov chains would reduce the dependence on the IM.

The earthquake dynamic inversion problem suffers from the so-called “curse of dimensionality” - the volume of the parameter space exponentially increases with the number of parameters. Further increasing the computational resources consumed ($>57,000$ GPU hr for this study) will likely be impermissible or at least highly inefficient because the error of the MCMC results decreases more slowly with the number of steps (Sokal, 1997).

Instead, future methodological improvements may be achieved by either (a) the introduction of advanced modeling methods or (b) reducing the number of model parameters. With respect to (a), new methods such as reduced-order modeling and machine learning techniques may aid in considerably speeding up the forward model calculation (Rekoske et al., 2023). Physics-based neural networks were recently applied to the rupture problem with rate-and-state friction and allow for dynamic parameter estimation as part of the training process (Rucker & Erickson, 2023). Recently, Stiernström et al. (2024) derived an adjoint-based inversion formulation for dynamic rupture, which may reduce the time-to-solution of dynamic source inversions but cannot provide model uncertainties. For (b), reducing the number of control points by, for example, decreasing their density at the edges of the fault or places with no expected slip will decrease the dimensionality of the forward problem. However, increasing the density of control points may open new possibilities to constrain the inversion, for example, by correlating dynamic parameters with properties of repeating small earthquakes (e.g., Abercrombie et al., 2020). Similarly, using a simpler linear-slip weakening friction law requires fewer model parameters and computational resources but can only capture coseismic rupture dynamics (e.g., Galović et al., 2019b). Lastly, integrating additional data sets, such as surface creep data (Langbein et al., 2006) or InSAR, given its much higher spatial resolution, may be promising future directions.

5. Conclusions

In this study, we conduct a joint dynamic rupture and afterslip finite-fault inversion of the 2004 M_w 6.0 Parkfield earthquake, resolving the spatial variability of prestress and fault friction parameters across time scales. Using the best-fitting model ensemble, we delineate the uncertainty bounds of dynamic model parameters and reveal their inherent trade-offs. The preferred dynamic model unifies the complexities of co- and postseismic fault slip, jointly constrained by seismic and geodetic observations.

We observe significant spatial heterogeneity in coseismic dynamic rupture and identify a pulse-like rupture phase followed by a crack-like rupture phase. The two distinct coseismic rupture phases are separated by a shallow strength barrier located 7–8 km northwest of the hypocenter, which nearly arrests coseismic slip and subsequently causes a pronounced gap in the 90-day afterslip evolution. Our joint rate-and-state framework elucidates distinct dynamic rupture termination mechanisms, which are closely tied to the subsequent evolution of afterslip. Dynamic rupture entering VS regions that host subsequent afterslip is a well-resolved and persistent feature of our

model ensemble. Across the entire area of fault slip, including regions hosting afterslip, the spatial average of $b - a$ levels at 0.000 (with a standard deviation of 0.0059). Postseismic slip rate functions mostly resemble crack-like behavior with rise times gradually increasing with distance to the edge of the coseismic rupture area. We detect a backward propagating afterslip front, which aligns with delayed aftershock activity located above the hypocenter. Our analysis provides data-constrained and physics-based estimates of source parameters and their interactions.

We observe areas of negative coseismic stress drop that may explain the occurrence of shallow aftershock clusters within the coseismic rupture area. The inferred friction drop aligns with a statically stronger and dynamically weaker Parkfield section of the SAF. The 10,500 best-fitting model ensemble's average coseismic radiation efficiency is 0.21, its coseismic stress drop is 2.73 MPa, and its average postseismic stress drop is 0.39 MPa, despite similarly large co- and postseismic moments. This study demonstrates how physics-based models using modern computational techniques can uncover new insights and unprecedented details of well-recorded earthquakes.

Conflict of Interest

The authors declare no conflicts of interest relevant to this study.

Data Availability Statement

All seismic data are obtained through the CESMD (Center for Engineering Strong Motion Data) web service and we only use stations from the California Strong Motion Instrumentation Program (CSMIP, California Geological Survey, 1972). We use processed coseismic and postseismic GPS data by Jiang et al. (2021a), which are publicly available (Jiang et al., 2021b). The FD3D_TSN (Premus et al., 2020) version and all required input files to run the dynamic source inversion of the 2004 Parkfield earthquake are available (Schliwa, 2024).

Acknowledgments

The manuscript greatly benefited from comments by Roland Bürgmann. We thank two anonymous reviewers, the Editor Rachel Abercrombie, and the anonymous Associate Editor for their constructive comments. This study was supported by the European Union's Horizon 2020 Research and Innovation Programme (TEAR, Grant 852992), Horizon Europe (ChEESE-2P, Grant 101093038, DT-GEO, Grant 101058129, and Geo-INQUIRE, Grant 101058518), the Deutsche Forschungsgemeinschaft (DFG, German Research Foundation, Grants 495931446, 518204048), the National Aeronautics and Space Administration (80NSSC20K0495), the National Science Foundation (Grants EAR-2225286, EAR-2121568, OAC-2139536, OAC-2311208) and the Statewide California Earthquake Center (SECE awards 22135, 23121). F. G. was supported by the Johannes Amos Comenius Programme (P JAC), project No. CZ.02.01.01/00/22_008/0004605, Natural and anthropogenic georisks. Computing resources were provided by the Institute of Geophysics of LMU Munich (Oeser et al., 2006). Open Access funding enabled and organized by Projekt DEAL.

References

- Abercrombie, R. E., Chen, X., & Zhang, J. (2020). Repeating earthquakes with remarkably repeatable ruptures on the San Andreas Fault at Parkfield. *Geophysical Research Letters*, 47(23). <https://doi.org/10.1029/2020gl089820>
- Allmann, B. P., & Shearer, P. M. (2007). A high-frequency secondary event during the 2004 Parkfield earthquake. *Science*, 318(5854), 1279–1283. <https://doi.org/10.1126/science.1146537>
- Allmann, B. P., & Shearer, P. M. (2009). Global variations of stress drop for moderate to large earthquakes. *Journal of Geophysical Research*, 114(B1). <https://doi.org/10.1029/2008jb005821>
- Ampuero, J.-P., & Rubin, A. M. (2008). Earthquake nucleation on rate and state faults – Aging and slip laws. *Journal of Geophysical Research*, 113(B1). <https://doi.org/10.1029/2007jb005082>
- Andrews, D. J. (1976). Rupture velocity of plane strain shear cracks. *Journal of Geophysical Research*, 81(32), 5679–5687. <https://doi.org/10.1029/jb081i032p05679>
- Bakun, W. H., Aagaard, B., Dost, B., Ellsworth, W., Hardebeck, J., Harris, R., et al. (2005). Implications for prediction and hazard assessment from the 2004 Parkfield earthquake. *Nature*, 437(7061), 969–974. <https://doi.org/10.1038/nature04067>
- Bakun, W. H., & Lindh, A. G. (1985). The Parkfield, California, earthquake prediction experiment. *Science*, 229(4714), 619–624. <https://doi.org/10.1126/science.229.4714.619>
- Bakun, W. H., & McEvilly, T. V. (1984). Recurrence models and Parkfield, California, earthquakes. *Journal of Geophysical Research*, 89(B5), 3051–3058. <https://doi.org/10.1029/jb089ib05p03051>
- Bao, H., Ampuero, J. P., Meng, L., Fielding, E., Liang, C., Milliner, C., et al. (2019). Early and persistent supershear rupture of the 2018 magnitude 7.5 Palu earthquake. *Nature Geoscience*, 12(3), 200–205. <https://doi.org/10.1038/s41561-018-0297-z>
- Barbot, S., Fialko, Y., & Bock, Y. (2009). Postseismic deformation due to the Mw 6.0 2004 Parkfield earthquake: Stress-driven creep on a fault with spatially variable rate-and-state friction parameters. *Journal of Geophysical Research*, 114(B7). <https://doi.org/10.1029/2008jb005748>
- Barbot, S., Lapusta, N., & Avouac, J.-P. (2012). Under the hood of the earthquake machine: Toward predictive modeling of the seismic cycle. *Science*, 336(6082), 707–710. <https://doi.org/10.1126/science.1218796>
- Barras, F., Thøgersen, K., Aharonov, E., & Renard, F. (2023). How do earthquakes stop? Insights from a minimal model of frictional rupture. *Journal of Geophysical Research: Solid Earth*, 128(8). <https://doi.org/10.1029/2022jb026070>
- Bilham, R. (2005). Coseismic strain and the transition to surface afterslip recorded by creepmeters near the 2004 Parkfield epicenter. *Seismological Research Letters*, 76(1), 49–57. <https://doi.org/10.1785/gssrl.76.1.49>
- Blanpied, M. L., Lockner, D. A., & Byerlee, J. D. (1991). Fault stability inferred from granite sliding experiments at hydrothermal conditions. *Geophysical Research Letters*, 18(4), 609–612. <https://doi.org/10.1029/91gl00469>
- Brengman, C. M. J., Barnhart, W. D., Mankin, E. H., & Miller, C. N. (2019). Earthquake-scaling relationships from geodetically derived slip distributions. *Bulletin of the Seismological Society of America*, 109(5), 1701–1715. <https://doi.org/10.1785/0120190048>
- Bruhat, L., Barbot, S., & Avouac, J.-P. (2011). Evidence for postseismic deformation of the lower crust following the 2004 Mw6.0 Parkfield earthquake. *Journal of Geophysical Research*, 116(B8), B08401. <https://doi.org/10.1029/2010jb008073>
- Brune, J. N. (1970). Tectonic stress and the spectra of seismic shear waves from earthquakes. *Journal of Geophysical Research*, 75(26), 4997–5009. <https://doi.org/10.1029/jb075i026p04997>
- Burridge, R., Conn, G., & Freund, L. B. (1979). The stability of a rapid mode II shear crack with finite cohesive traction. *Journal of Geophysical Research*, 84(B5), 2210–2222. <https://doi.org/10.1029/jb084ib05p02210>
- Byerlee, J. D. (1978). Friction of rocks. *Pure and Applied Geophysics*, 116(4–5), 615–626. <https://doi.org/10.1007/bf00876528>

- California Geological Survey. (1972). California strong motion instrumentation program. *International Federation of Digital Seismograph Networks*. <https://doi.org/10.7914/B34Q-BB70>
- Cattania, C., Hainzl, S., Wang, L., Enescu, B., & Roth, F. (2015). Aftershock triggering by postseismic stresses: A study based on Coulomb rate-and-state models. *Journal of Geophysical Research: Solid Earth*, *120*(4), 2388–2407. <https://doi.org/10.1002/2014jb011500>
- Chang, S.-H., Avouac, J.-P., Barbot, S., & Lee, J.-C. (2013). Spatially variable fault friction derived from dynamic modeling of aseismic afterslip due to the 2004 Parkfield earthquake. *Journal of Geophysical Research: Solid Earth*, *118*(7), 3431–3447. <https://doi.org/10.1002/jgrb.50231>
- Churchill, R. M., Werner, M. J., Biggs, J., & Fagereng, Å. (2022). Relative afterslip moment does not correlate with aftershock productivity: Implications for the relationship between afterslip and aftershocks. *Geophysical Research Letters*, *49*(24). <https://doi.org/10.1029/2022gl101165>
- Churchill, R. M., Werner, M. J., Biggs, J., & Fagereng, Å. (2024). Spatial relationships between coseismic slip, aseismic afterslip, and on-fault aftershock density in continental earthquakes. *Journal of Geophysical Research: Solid Earth*, *129*(1). <https://doi.org/10.1029/2023jb027168>
- Cocco, M., Aretusini, S., Cornelio, C., Nielsen, S. B., Spagnuolo, E., Tinti, E., & Di Toro, G. (2023). Fracture energy and breakdown work during earthquakes. *Annual Review of Earth and Planetary Sciences*, *51*(1), 217–252. <https://doi.org/10.1146/annurev-earth-071822-100304>
- Cocco, M., & Bizzarri, A. (2002). On the slip-weakening behavior of rate- and state dependent constitutive laws. *Geophysical Research Letters*, *29*(11). <https://doi.org/10.1029/2001gl013999>
- Cotton, F., & Coutant, O. (1997). Dynamic stress variations due to shear faults in a plane-layered medium. *Geophysical Journal International*, *128*(3), 676–688. <https://doi.org/10.1111/j.1365-246x.1997.tb05328.x>
- Custódio, S., Liu, P., & Archuleta, R. J. (2005). The 2004 Mw6.0 Parkfield, California, earthquake: Inversion of near-source ground motion using multiple data sets. *Geophysical Research Letters*, *32*(23). <https://doi.org/10.1029/2005gl024417>
- Custódio, S., Page, M. T., & Archuleta, R. J. (2009). Constraining earthquake source inversions with GPS data: 2. A two-step approach to combine seismic and geodetic data sets. *Journal of Geophysical Research*, *114*(B1). <https://doi.org/10.1029/2008jb005746>
- Dalguer, L. A., & Day, S. M. (2007). Staggered-grid split-node method for spontaneous rupture simulation. *Journal of Geophysical Research*, *112*(B2). <https://doi.org/10.1029/2006jb004467>
- Das, S. (2015). Supershear earthquake ruptures – Theory, methods, laboratory experiments and fault superhighways: An update. *Geotechnical, Geological and Earthquake Engineering*, *39*, 1–20. https://doi.org/10.1007/978-3-319-16964-4_1
- Day, S. M., Dalguer, L. A., Lapusta, N., & Liu, Y. (2005). Comparison of finite difference and boundary integral solutions to three-dimensional spontaneous rupture. *Journal of Geophysical Research*, *110*(B12). <https://doi.org/10.1029/2005jb003813>
- Dieterich, J. H. (1992). Earthquake nucleation on faults with rate-and state-dependent strength. *Tectonophysics*, *211*(1–4), 115–134. [https://doi.org/10.1016/0040-1951\(92\)90055-b](https://doi.org/10.1016/0040-1951(92)90055-b)
- Fletcher, J. B., Spudich, P., & Baker, L. M. (2006). Rupture propagation of the 2004 Parkfield, California, earthquake from observations at the UPSAR. *Bulletin of the Seismological Society of America*, *96*(4B), S129–S142. <https://doi.org/10.1785/0120050812>
- Freed, A. M. (2007). Afterslip (and only afterslip) following the 2004 Parkfield, California, earthquake. *Geophysical Research Letters*, *34*(6). <https://doi.org/10.1029/2006gl029155>
- Freund, L. B. (1979). The mechanics of dynamic shear crack propagation. *Journal of Geophysical Research*, *84*(B5), 2199–2209. <https://doi.org/10.1029/jb084ib05p02199>
- Fukuyama, E., & Mikumo, T. (1993). Dynamic rupture analysis: Inversion for the source process of the 1990 Izu-Oshima, Japan, earthquake (M = 6.5). *Journal of Geophysical Research*, *98*(B4), 6529–6542. <https://doi.org/10.1029/92jb02451>
- Gabriel, A.-A., Ampuero, J.-P., Dalguer, L. A., & Mai, P. M. (2012). The transition of dynamic rupture styles in elastic media under velocity-weakening friction. *Journal of Geophysical Research*, *117*(B9). <https://doi.org/10.1029/2012jb009468>
- Gabriel, A.-A., Ampuero, J.-P., Dalguer, L. A., & Mai, P. M. (2013). Source properties of dynamic rupture pulses with off-fault plasticity. *Journal of Geophysical Research: Solid Earth*, *118*(8), 4117–4126. <https://doi.org/10.1002/jgrb.50213>
- Gabriel, A.-A., Garagash, D. I., Palgunadi, K. H., & Mai, P. M. (2024). Fault size-dependent fracture energy explains multiscale seismicity and cascading earthquakes. *Science*, *385*(6707). <https://doi.org/10.1126/science.adj9587>
- Gallovič, F. (2008). Heterogeneous Coulomb stress perturbation during earthquake cycles in a 3D rate-and-state fault model. *Geophysical Research Letters*, *35*(21). <https://doi.org/10.1029/2008gl035614>
- Gallovič, F., & Ampuero, J.-P. (2015). A new strategy to compare inverted rupture models exploiting the Eigenstructure of the inverse problem. *Seismological Research Letters*, *86*(6), 1679–1689. <https://doi.org/10.1785/0220150096>
- Gallovič, F., Valentová, L., Ampuero, J.-P., & Gabriel, A.-A. (2019a). Bayesian dynamic finite-fault inversion: 1. Method and synthetic test. *Journal of Geophysical Research: Solid Earth*, *124*(7), 6949–6969. <https://doi.org/10.1029/2019jb017510>
- Gallovič, F., Valentová, L., Ampuero, J.-P., & Gabriel, A.-A. (2019b). Bayesian dynamic finite-fault inversion: 2. Application to the 2016 Mw 6.2 Amatrice, Italy, earthquake. *Journal of Geophysical Research: Solid Earth*, *124*(7), 6970–6988. <https://doi.org/10.1029/2019jb017512>
- Gallovič, F., Zahradník, J., Plicka, V., Sokos, E., Evangelidis, C., Fountoulakis, I., & Turhan, F. (2020). Complex rupture dynamics on an immature fault during the 2020 Mw 6.8 Elazığ earthquake, Turkey. *Commun. Earth Environ.*, *1*, 40. <https://doi.org/10.1038/s43247-020-00038-x>
- Guatteri, M., Mai, P. M., & Beroza, G. C. (2004). A pseudo-dynamic approximation to dynamic rupture models for strong ground motion prediction. *Bulletin of the Seismological Society of America*, *94*(6), 2051–2063. <https://doi.org/10.1785/0120040037>
- Hallo, M., & Gallovič, F. (2016). Fast and cheap approximation of Green function uncertainty for waveform-based earthquake source inversions. *Geophysical Journal International*, *207*(2), 1012–1029. <https://doi.org/10.1093/gji/ggw320>
- Harris, R. A., Barall, M., Aagaard, B., Ma, S., Roten, D., Olsen, K., et al. (2018). A suite of exercises for verifying dynamic earthquake rupture codes. *Seismological Research Letters*, *89*(3), 1146–1162. <https://doi.org/10.1785/0220170222>
- Heaton, T. H. (1990). Evidence for and implications of self-healing pulses of slip in earthquake rupture. *Physics of the Earth and Planetary Interiors*, *64*(1), 1–20. [https://doi.org/10.1016/0031-9201\(90\)90002-f](https://doi.org/10.1016/0031-9201(90)90002-f)
- Heinecke, A., Breuer, A., Rettenberger, S., Bader, M., Gabriel, A.-A., Pelties, C., et al. (2014). Petascale high order dynamic rupture earthquake simulations on heterogeneous supercomputers. In *SC '14: Proceedings of the International Conference for High Performance Computing, Networking, Storage and Analysis*.
- Hickman, S., & Zoback, M. (2004). Stress orientations and magnitudes in the SAFOD pilot hole. *Geophysical Research Letters*, *31*(15). <https://doi.org/10.1029/2004gl020043>
- Ide, S., Beroza, G. C., & Mcguire, J. J. (2005). Imaging earthquake source complexity. In *Seismic Earth: Array analysis of broadband seismograms* (pp. 117–135). American Geophysical Union (AGU).
- Jiang, J., Bock, Y., & Klein, E. (2021a). Coevolving early afterslip and aftershock signatures of a San Andreas Fault rupture. *Science Advances*, *7*(15). <https://doi.org/10.1126/sciadv.abc1606>

- Jiang, J., Bock, Y., & Klein, E. (2021b). Data and models for 'coevolving early afterslip and aftershock signatures of a San Andreas Fault rupture' [Dataset]. *Zenodo*. <https://doi.org/10.5281/zenodo.4278477>
- Johanson, I. A., Fielding, E. J., Rolandone, F., & Bürgmann, R. (2006). Coseismic and postseismic slip of the 2004 Parkfield earthquake from space-geodetic data. *Bulletin of the Seismological Society of America*, 96(4B), S269–S282. <https://doi.org/10.1785/0120050818>
- Johnson, K. M., Bürgmann, R., & Larson, K. (2006). Frictional properties on the San Andreas Fault near Parkfield, California, inferred from models of afterslip following the 2004 earthquake. *Bulletin of the Seismological Society of America*, 96(4B), S321–S338. <https://doi.org/10.1785/0120050808>
- Johnson, K. M., Shelly, D. R., & Bradley, A. M. (2013). Simulations of tremor-related creep reveal a weak crustal root of the San Andreas Fault. *Geophysical Research Letters*, 40(7), 1300–1305. <https://doi.org/10.1002/grl.50216>
- Jolivet, R., Simons, M., Agram, P. S., Duputel, Z., & Shen, Z.-K. (2015). Aseismic slip and seismogenic coupling along the central San Andreas Fault. *Geophysical Research Letters*, 42(2), 297–306. <https://doi.org/10.1002/2014gl062222>
- Kagan, Y. Y., & Houston, H. (2005). Relation between mainshock rupture process and Omori's law for aftershock moment release rate. *Geophysical Journal International*, 163(3), 1039–1048. <https://doi.org/10.1111/j.1365-246x.2005.02772.x>
- Kaneko, Y., & Shearer, P. M. (2014). Seismic source spectra and estimated stress drop derived from cohesive-zone models of circular subshear rupture. *Geophysical Journal International*, 197(2), 1002–1015. <https://doi.org/10.1093/gji/ggu030>
- Ke, C.-Y., McLaskey, G. C., & Kammer, D. S. (2018). Rupture termination in laboratory-generated earthquakes. *Geophysical Research Letters*, 45(23). <https://doi.org/10.1029/2018gl080492>
- Kim, A., & Dreger, D. S. (2008). Rupture process of the 2004 Parkfield earthquake from near-fault seismic waveform and geodetic records. *Journal of Geophysical Research*, 113(B7). <https://doi.org/10.1029/2007jb005115>
- Kostka, F., & Gallovič, F. (2016). Static Coulomb stress load on a three-dimensional rate-and-state fault: Possible explanation of the anomalous delay of the 2004 Parkfield earthquake. *Journal of Geophysical Research: Solid Earth*, 121(5), 3517–3533. <https://doi.org/10.1002/2015jb012646>
- Krenz, L., Uphoff, C., Ulrich, T., Gabriel, A.-A., Abrahams, L. S., Dunham, E. M., & Bader, M. (2021). 3D acoustic-elastic coupling with gravity: The dynamics of the 2018 Palu, Sulawesi earthquake and tsunami. In *Proceedings of the international conference for high performance computing, networking, storage and analysis*. Association for Computing Machinery.
- Lachenbruch, A. H., & Sass, J. H. (1980). Heat flow and energetics of the San Andreas Fault Zone. *Journal of Geophysical Research*, 85(B11), 6185–6222. <https://doi.org/10.1029/jb085ib11p06185>
- Lambert, V., Lapusta, N., & Perry, S. (2021). Propagation of large earthquakes as self-healing pulses or mild cracks. *Nature*, 591(7849), 252–258. <https://doi.org/10.1038/s41586-021-03248-1>
- Langbein, J., Borchardt, R., Dreger, D., Fletcher, J., Hardebeck, J. L., Hellweg, M., et al. (2005). Preliminary report on the 28 September 2004, M 6.0 Parkfield, California earthquake. *Seismological Research Letters*, 76(1), 10–26. <https://doi.org/10.1785/gssrl.76.1.10>
- Langbein, J., Murray, J. R., & Snyder, H. A. (2006). Coseismic and initial postseismic deformation from the 2004 Parkfield, California, earthquake, observed by global positioning system, electronic distance meter, creepmeters, and borehole strainmeters. *Bulletin of the Seismological Society of America*, 96(4B), S304–S320. <https://doi.org/10.1785/0120050823>
- Lewis, M. A., & Ben-Zion, Y. (2010). Diversity of fault zone damage and trapping structures in the Parkfield section of the San Andreas Fault from comprehensive analysis of near fault seismograms. *Geophysical Journal International*, 183(3), 1579–1595. <https://doi.org/10.1111/j.1365-246x.2010.04816.x>
- Li, Y.-G., Leary, P., Aki, K., & Malin, P. (1990). Seismic trapped modes in the Oroville and San Andreas Fault zones. *Science*, 249(4970), 763–766. <https://doi.org/10.1126/science.249.4970.763>
- Lienkaemper, J. J., Baker, B., & McFarland, F. S. (2006). Surface slip associated with the 2004 Parkfield, California, earthquake measured on alignment arrays. *Bulletin of the Seismological Society of America*, 96(4B), S239–S249. <https://doi.org/10.1785/0120050806>
- Lisowski, M., Savage, J. C., & Prescott, W. H. (1991). The velocity field along the San Andreas Fault in central and southern California. *Journal of Geophysical Research*, 96(B5), 8369–8389. <https://doi.org/10.1029/91jb00199>
- Liu, P., Custódio, S., & Archuleta, R. J. (2006). Kinematic inversion of the 2004 M 6.0 Parkfield earthquake including an approximation to site effects. *Bulletin of the Seismological Society of America*, 96(4B), S143–S158. <https://doi.org/10.1785/0120050826>
- Lockner, D., Morrow, C., Moore, D., & Hickman, S. (2011). Low strength of deep San Andreas Fault gouge from SAFOD core. *Nature*, 472(7341), 82–85. <https://doi.org/10.1038/nature09927>
- Lui, S. K. Y., & Lapusta, N. (2018). Modeling high stress drops, scaling, interaction, and irregularity of repeating earthquake sequences near Parkfield. *Journal of Geophysical Research: Solid Earth*, 123(12). <https://doi.org/10.1029/2018jb016472>
- Ma, S., Custódio, S., Archuleta, R. J., & Liu, P. (2008). Dynamic modeling of the 2004 Mw 6.0 Parkfield, California, earthquake. *Journal of Geophysical Research*, 113(B2). <https://doi.org/10.1029/2007jb005216>
- Madariaga, R. (1976). Dynamics of an expanding circular fault. *Bulletin of the Seismological Society of America*, 66(3), 639–666. <https://doi.org/10.1785/bssa0660030639>
- Madariaga, R. (1977). High-frequency radiation from crack (stress drop) models of earthquake faulting. *Geophysical Journal International*, 51(3), 625–651. <https://doi.org/10.1111/j.1365-246x.1977.tb04211.x>
- Madden, E. H., Ulrich, T., & Gabriel, A.-A. (2022). The state of pore fluid pressure and 3-D megathrust earthquake dynamics. *Journal of Geophysical Research: Solid Earth*, 127(4). <https://doi.org/10.1029/2021jb023382>
- Mai, P., Galis, M., Thingbaijam, K. K., Vyas, J., & Dunham, E. (2017). Accounting for fault roughness in pseudo-dynamic ground-motion simulations. *Pure and Applied Geophysics*, 174, 95–126. https://doi.org/10.1007/978-3-319-72709-7_7
- Mikumo, T., & Miyatake, T. (1995). Heterogeneous distribution of dynamic stress drop and relative fault strength recovered from the results of waveform inversion: The 1984 Morgan Hill, California, earthquake. *Bulletin of the Seismological Society of America*, 85(1), 178–193. <https://doi.org/10.1785/bssa0850010178>
- Murray, J., & Langbein, J. (2006). Slip on the San Andreas Fault at Parkfield, California, over two earthquake cycles, and the implications for seismic hazard. *Bulletin of the Seismological Society of America*, 96(4B), S283–S303. <https://doi.org/10.1785/0120050820>
- Neves, M., Peng, Z., & Lin, G. (2022). A high-resolution earthquake catalog for the 2004 Mw 6 Parkfield earthquake sequence using a matched filter technique. *Seismological Research Letters*, 94(1), 507–521. <https://doi.org/10.1785/0220220206>
- Noda, H., Dunham, E. M., & Rice, J. R. (2009). Earthquake ruptures with thermal weakening and the operation of major faults at low overall stress levels. *Journal of Geophysical Research*, 114(B7). <https://doi.org/10.1029/2008jb006143>
- Noda, H., & Lapusta, N. (2010). 3D simulations of long-term fault slip with dynamic weakening: Relation between locked patches and earthquake-induced stress changes. In *Workshop on earthquake source dynamics: Data and data-constrained numerical modeling*.
- Oeser, J., Bunge, H.-P., & Mohr, M. (2006). Cluster design in the Earth sciences tethys. In M. Gerndt & D. Kranzlmüller (Eds.), *High performance computing and communications*. Springer Berlin Heidelberg.

- Oglesby, D. D., & Day, S. M. (2002). Stochastic Fault stress: Implications for fault dynamics and ground motion. *Bulletin of the Seismological Society of America*, 92(8), 3006–3021. <https://doi.org/10.1785/0120010249>
- Okada, Y. (1985). Surface deformation due to shear and tensile faults in a half-space. *Bulletin of the Seismological Society of America*, 75(4), 1135–1154. <https://doi.org/10.1785/bssa0750041135>
- Olsen, K. B., Day, S. M., & Bradley, C. R. (2003). Estimation of Q for long-period (>2 sec) waves in the Los Angeles Basin. *Bulletin of the Seismological Society of America*, 93(2), 627–638. <https://doi.org/10.1785/0120020135>
- Page, M. T., Custódio, S., Archuleta, R. J., & Carlson, J. M. (2009). Constraining earthquake source inversions with GPS data: I. Resolution-Based removal of artifacts. *Journal of Geophysical Research*, 114(B1). <https://doi.org/10.1029/2007jb005449>
- Page, M. T., Mai, P. M., & Schorlemmer, D. (2011). Testing earthquake source inversion methodologies. *Eos, Transactions American Geophysical Union*, 92(9), 75. <https://doi.org/10.1029/2011eo090007>
- Palgunadi, K. H., Gabriel, A.-A., Garagash, D. I., Ulrich, T., & Mai, P. M. (2024). Rupture dynamics of cascading earthquakes in a multiscale fracture network. *Journal of Geophysical Research: Solid Earth*, 129(3). <https://doi.org/10.1029/2023jb027578>
- Peng, Z., & Zhao, P. (2009). Migration of early aftershocks following the 2004 Parkfield earthquake. *Nature Geoscience*, 2(12), 877–881. <https://doi.org/10.1038/ngeo0697>
- Perrin, G., Rice, J. R., & Zheng, G. (1995). Self-healing slip pulse on a frictional surface. *Journal of the Mechanics and Physics of Solids*, 43(9), 1461–1495. [https://doi.org/10.1016/0022-5096\(95\)00036-i](https://doi.org/10.1016/0022-5096(95)00036-i)
- Peyrat, S., & Olsen, K. B. (2004). Nonlinear dynamic rupture inversion of the 2000 Western Tottori, Japan, earthquake. *Geophysical Research Letters*, 31(5). <https://doi.org/10.1029/2003gl019058>
- Premus, J., Gallovič, F., & Ampuero, J.-P. (2022). Bridging time scales of faulting: From coseismic to postseismic slip of the M_w 6.0 2014 South Napa, California earthquake. *Science Advances*, 8(38). <https://doi.org/10.1126/sciadv.abq2536>
- Premus, J., Gallovič, F., Hanyk, L., & Gabriel, A. (2020). FD3D_TSN: A fast and simple code for dynamic rupture simulations with GPU acceleration. *Seismological Research Letters*, 91(5), 2881–2889. <https://doi.org/10.1785/0220190374>
- Press, F. (1968). Earth models obtained by Monte Carlo Inversion. *Journal of Geophysical Research*, 73(16), 5223–5234. <https://doi.org/10.1029/jb073i016p05223>
- Pulido, N., & Dalguer, L. A. (2009). Estimation of the high-frequency radiation of the 2000 Tottori (Japan) earthquake based on a dynamic model of fault rupture: Application to the strong ground motion simulation. *Bulletin of the Seismological Society of America*, 99(4), 2305–2322. <https://doi.org/10.1785/0120080165>
- Quin, H. (1990). Dynamic stress drop and rupture dynamics of the October 15, 1979 Imperial Valley, California, earthquake. *Tectonophysics*, 175(1–3), 93–117. [https://doi.org/10.1016/0040-1951\(90\)90132-r](https://doi.org/10.1016/0040-1951(90)90132-r)
- Rekoske, J. M., Gabriel, A.-A., & May, D. A. (2023). Instantaneous physics-based ground motion maps using reduced-order modeling. *Journal of Geophysical Research: Solid Earth*, 128(8). <https://doi.org/10.1029/2023jb026975>
- Rice, J. R. (1992). Fault stress states, pore pressure distributions, and the weakness of the San Andreas Fault. In B. Evans & T. Fong Wong (Eds.), *Fault mechanics and transport properties of rocks* (Vol. 51, pp. 475–503). Academic Press.
- Rice, J. R. (1993). Spatio-temporal complexity of slip on a fault. *Journal of Geophysical Research*, 98(B6), 9885–9907. <https://doi.org/10.1029/93jb00191>
- Rucker, C., & Erickson, B. A. (2023). Physics-informed deep learning of rate-and-state fault friction.
- Ruina, A. (1983). Slip instability and state variable friction laws. *Journal of Geophysical Research*, 88(B12), 10359–10370. <https://doi.org/10.1029/jb088ib12p10359>
- Rymer, M. J., Tinsley, I., John, C., Treiman, J. A., Arrowsmith, J. R., Clahan, K. B., et al. (2006). Surface Fault slip associated with the 2004 Parkfield, California, earthquake. *Bulletin of the Seismological Society of America*, 96(4B), S11–S27. <https://doi.org/10.1785/0120050830>
- Schliwa, N. (2024). FD3D_TSN/2004Parkfield [Software]. *Zenodo*. <https://doi.org/10.5281/zenodo.11072717>
- Schliwa, N., & Gabriel, A. (2023). Equivalent near-field corner frequency analysis of 3D dynamic rupture simulations reveals dynamic source effects. *Seismological Research Letters*, 95(2A), 900–924. <https://doi.org/10.1785/0220230225>
- Schmedes, J., Archuleta, R. J., & Lavallée, D. (2010). Correlation of earthquake source parameters inferred from dynamic rupture simulations. *Journal of Geophysical Research*, 115(B3). <https://doi.org/10.1029/2009jb006689>
- Schmedes, J., Archuleta, R. J., & Lavallée, D. (2012). A kinematic rupture model generator incorporating spatial interdependency of earthquake source parameters. *Geophysical Journal International*, 192(3), 1116–1131. <https://doi.org/10.1093/gji/ggs021>
- Shakal, A., Haddadi, H., Graizer, V., Lin, K., & Huang, M. (2006). Some key features of the strong-motion data from the M 6.0 Parkfield, California, earthquake of 28 September 2004. *Bulletin of the Seismological Society of America*, 96(4B), S90–S118. <https://doi.org/10.1785/0120050817>
- Shelly, D. R., & Johnson, K. M. (2011). Tremor reveals stress shadowing, deep postseismic creep, and depth-dependent slip recurrence on the lower-crustal San Andreas fault near Parkfield. *Geophysical Research Letters*, 38(13). <https://doi.org/10.1029/2011gl047863>
- Shi, Z., & Day, S. M. (2013). Rupture dynamics and ground motion from 3-D rough-fault simulations. *Journal of Geophysical Research: Solid Earth*, 118(3), 1122–1141. <https://doi.org/10.1002/jgrb.50094>
- Simpson, R. W., Barall, M., Langbein, J., Murray, J. R., & Rymer, M. J. (2006). San Andreas Fault geometry in the Parkfield, California, region. *Bulletin of the Seismological Society of America*, 96(4B), S28–S37. <https://doi.org/10.1785/0120050824>
- Sokal, A. (1997). Monte Carlo methods in statistical mechanics: Foundations and new algorithms. In *Functional integration: Basics and applications*. Springer US.
- Song, S. G., Dalguer, L. A., & Mai, P. M. (2013). Pseudo-dynamic source modelling with 1-point and 2-point statistics of earthquake source parameters. *Geophysical Journal International*, 196(3), 1770–1786. <https://doi.org/10.1093/gji/ggt479>
- Stiemström, V., Almqvist, M., & Dunham, E. M. (2024). Adjoint-based inversion for stress and frictional parameters in earthquake modeling. *Journal of Computational Physics*, 519, 113447. <https://doi.org/10.1016/j.jcp.2024.113447>
- Suppe, J. (2014). Fluid overpressures and strength of the sedimentary upper crust. *Journal of Structural Geology*, 69, 481–492. <https://doi.org/10.1016/j.jsg.2014.07.009>
- Taufiqurrahman, T., Gabriel, A.-A., Li, D., Ulrich, T., Li, B., Carena, S., et al. (2023). Dynamics, interactions and delays of the 2019 Ridgecrest rupture sequence. *Nature*, 618(7964), 308–315. <https://doi.org/10.1038/s41586-023-05985-x>
- Thomas, M. Y., Lapusta, N., Noda, H., & Avouac, J.-P. (2014). Quasi-dynamic versus fully dynamic simulations of earthquakes and aseismic slip with and without enhanced coseismic weakening. *Journal of Geophysical Research: Solid Earth*, 119(3), 1986–2004. <https://doi.org/10.1002/2013jb010615>
- Thurber, C., Zhang, H., Waldhauser, F., Hardebeck, J., Michael, A., & Eberhart-Phillips, D. (2006). Three-dimensional compressional wavespeed model, earthquake relocations, and focal mechanisms for the Parkfield, California, region. *Bulletin of the Seismological Society of America*, 96(4B), S38–S49. <https://doi.org/10.1785/0120050825>

- Tinti, E., Casarotti, E., Ulrich, T., Taufiqurrahman, T., Li, D., & Gabriel, A.-A. (2021). Constraining families of dynamic models using geological, geodetic and strong ground motion data: The Mw 6.5, October 30th, 2016, Norcia earthquake, Italy. *Earth and Planetary Science Letters*, 576, 117237. <https://doi.org/10.1016/j.epsl.2021.117237>
- Titus, S. J., DeMets, C., & Tikoff, B. (2005). New slip rate estimates for the creeping segment of the San Andreas Fault, California. *Geology*, 33(3), 205. <https://doi.org/10.1130/g21107.1>
- Tong, X., Sandwell, D. T., & Smith-Konter, B. (2013). High-resolution interseismic velocity data along the San Andreas Fault from GPS and InSAR. *Journal of Geophysical Research: Solid Earth*, 118(1), 369–389. <https://doi.org/10.1029/2012jb009442>
- Twardzik, C., Das, S., & Madariaga, R. (2014). Inversion for the physical parameters that control the source dynamics of the 2004 Parkfield earthquake. *Journal of Geophysical Research: Solid Earth*, 119(9), 7010–7027. <https://doi.org/10.1002/2014jb011238>
- Twardzik, C., Madariaga, R., Das, S., & Custódio, S. (2012). Robust features of the source process for the 2004 Parkfield, California, earthquake from strong-motion seismograms. *Geophysical Journal International*, 191. <https://doi.org/10.1111/j.1365-246x.2012.05653.x>
- Ulrich, T., Gabriel, A.-A., Ampuero, J.-P., & Xu, W. (2019). Dynamic viability of the 2016 Mw 7.8 Kaikōura earthquake cascade on weak crustal faults. *Nature Communications*, 10(1), 1213. <https://doi.org/10.1038/s41467-019-09125-w>
- Uphoff, C., May, D. A., & Gabriel, A.-A. (2022). A discontinuous Galerkin method for sequences of earthquakes and aseismic slip on multiple faults using unstructured curvilinear grids. *Geophysical Journal International*, 233(1), 586–626. <https://doi.org/10.1093/gji/ggac467>
- Uphoff, C., Rettenberger, S., Bader, M., Madden, E. H., Ulrich, T., Wollherr, S., & Gabriel, A.-A. (2017). Extreme scale multi-physics simulations of the tsunamigenic 2004 sumatra megathrust earthquake. In *Proceedings of the international conference for high performance computing, networking, storage and analysis*. Association for Computing Machinery.
- Utsu, T., Ogata, Y., & S. R., & Matsu'ura. (1995). The centenary of the Omori formula for a decay law of aftershock activity. *Journal of Physics of the Earth*, 43(1), 1–33. <https://doi.org/10.4294/jpe1952.43.1>
- Vavra, E., Fialko, Y., Rockwell, T. K., Bilham, R., Stepancikova, P., Stemberk, J., et al. (2023). *Characteristic slow-slip events on the superstition hills fault, southern California*. ESS Open Archive.
- Vyas, J. C., Gabriel, A., Ulrich, T., Mai, P. M., & Ampuero, J. (2023). How does thermal pressurization of pore fluids affect 3D strike-slip earthquake dynamics and ground motions? *Bulletin of the Seismological Society of America*, 113(5), 1992–2008. <https://doi.org/10.1785/0120220205>
- Wang, R., Lorenzo-Martín, F., & Roth, F. (2003). Computation of deformation induced by earthquakes in a multi-layered elastic crust—FORTRAN programs EDGRN/EDCMP. *Computers & Geosciences*, 29(2), 195–207. [https://doi.org/10.1016/s0098-3004\(02\)00111-5](https://doi.org/10.1016/s0098-3004(02)00111-5)
- Wang, R., Lorenzo-Martín, F., & Roth, F. (2006). PSGRN/PSCMP—A new code for calculating co- and post-seismic deformation, geoid and gravity changes based on the viscoelastic-gravitational dislocation theory. *Computers & Geosciences*, 32(4), 527–541. <https://doi.org/10.1016/j.cageo.2005.08.006>
- Wen, Y., Cai, J., He, K., & Xu, C. (2024). Dynamic rupture of the 2021 MW 7.4 Maduo earthquake: An intra-block event controlled by fault geometry. *Journal of Geophysical Research: Solid Earth*, 129(1). <https://doi.org/10.1029/2023jb027247>
- Williams, C. F., Grubb, F. V., & Galanis, S. P. Jr. (2004). Heat flow in the SAFOD pilot hole and implications for the strength of the San Andreas Fault. *Geophysical Research Letters*, 31(15). <https://doi.org/10.1029/2003gl019352>
- Zeng, X., Thurber, C. H., Shelly, D. R., Harrington, R. M., Cochran, E. S., Bennington, N. L., et al. (2016). 3-D P- and S-wave velocity structure and low-frequency earthquake locations in the Parkfield, California region. *Geophysical Journal International*, 206(3), 1574–1585. <https://doi.org/10.1093/gji/ggw217>
- Zhang, J., Chen, X., & Abercrombie, R. E. (2022). Spatiotemporal variability of earthquake source parameters at Parkfield, California, and their relationship with the 2004 M6 earthquake. *Journal of Geophysical Research: Solid Earth*, 127(6). <https://doi.org/10.1029/2021jb022851>
- Zhao, Z., & Yue, H. (2023). A two-step inversion for fault frictional properties using a temporally varying afterslip model and its application to the 2019 Ridgecrest earthquake. *Earth and Planetary Science Letters*, 602, 117932. <https://doi.org/10.1016/j.epsl.2022.117932>
- Zheng, G., & Rice, J. R. (1998). Conditions under which velocity-weakening friction allows a self-healing versus a cracklike mode of rupture. *Bulletin of the Seismological Society of America*, 88(6), 1466–1483. <https://doi.org/10.1785/bssa0880061466>